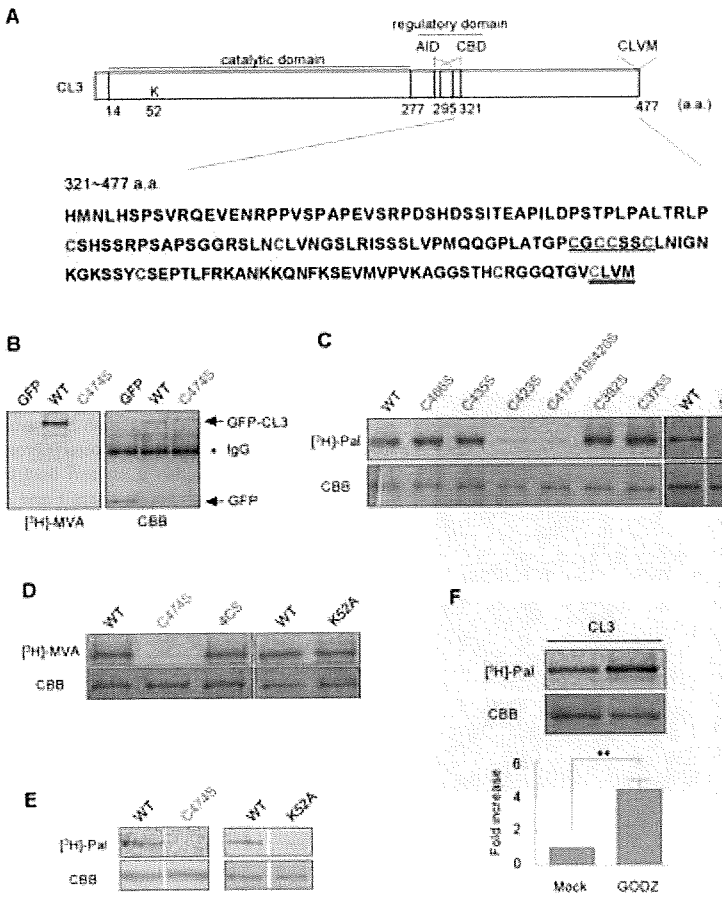

Figure 1. The C-Terminal Region of CL3 Is Covalently Modified by a Dual Lipidification Mechanism that Involves Prenylation of the CAAX Motif and a Subsequent Activity-Regulated Palmitoylation

(A) Domain structure of CL3 (upper panel) and amino acid sequence of its C-terminal end (lower panel). The numbers show the position of amino acid residues. In addition to a classical prenylation site at the Cys-474 residue (in blue) of the C-terminal CAAX motif (double underline), the unique C-terminal region of CL3 contained multiple Cys residues (in red and green), which constituted potential palmitoylation sites. Among them, four neighboring Cys (in red and underlined) were experimentally validated as critical residues for palmitoylation, as shown also in (C). AID, autoinhibitory domain; CBD, Ca^{2+}/calmodulin-binding domain.

(B) Prenylation of the CAAX motif of CL3. Immunoprecipitates for each sample were obtained using an anti-GFP antibody and examined by SDS-PAGE followed by autoradiographic exposure. [^{3}H]-mevalonate ([^{3}H]-MVA) incorporation (left) was detected in a wild-type GFP-CL3 (WT), but not in a CAAX motif mutant (C474S) or GFP alone. The amount of loaded proteins in each lane was comparable, as shown by CBB staining (right). The mobility of GFP-CL3 and GFP are indicated by arrows, and the heavy chain of the IgG used for immunoprecipitation is shown by an asterisk.

(C) Determination of critical palmitoylated Cys residues on CL3. Incorporation of [^{3}H]-palmitate ([^{3}H]-Pal) was observed in wild-type GFP-CL3 (WT). Incorporation of [^{3}H]-palmitate was significantly diminished in two mutants (in red), C417/419/420S (triple Cys-to-Ser substitution at residues 417, 419, and 420) and C423S, indicating the existence of multiple Cys residues critical for palmitoylation. Unaffected mutants are shown in green. A quadruple mutant (4CS) with a quadruple substitution had the least amount of [^{3}H]-palmitate incorporation and was considered to be a palmitoylation-deficient mutant (4CS).

(D) Unchanged level of prenylation on both a palmitoylation-deficient (4CS) and a kinase-dead (K52A, a Lys residue in the ATP-binding pocket replaced with an Ala) mutant of CL3.

(E) A decrease in palmitoylation was observed in a prenylation-deficient mutant (C474S), as well as a kinase-inactive mutant (K52A).

(F) Coexpression of HA-GODZ, a neuronal palmitoyl acyl transferase, led to a significant increase in CL3 palmitoylation by 4.32 ± 0.55 fold (n = 5). **$p < 0.01$ by paired t test.

increase (4.3 ± 0.55, n = 5) in the amount of palmitate incorporation (Figure 1F).

We previously found that prenylation per se may be necessary for membrane anchoring and for trafficking to diverse membrane compartments, such as the Golgi apparatus or the plasma membranes (Takemoto-Kimura et al., 2003). To test whether an additional palmitoylation may help to redistribute CL3 into specific membrane signalosomes such as those enriched at lipid rafts (Anderson and Jacobson, 2002), we expressed GFP-tagged CL3 (GFP-CL3) in cultured cortical neurons using a lentiviral vector driven by a synapsin I promoter. Consistent with our hypothesis, CL3 cofractionated with the lipid raft markers, caveolin-2 and flotillin-1, in the Triton X-100-insoluble low-density membrane fractions (Figure 2A). We next directly visualized raft-inserted CL3 localization in cultured neurons treated with 0.1% Triton X-100, as any residual GFP signal should then be indicative of the presence of CL3 in detergent-resistant membrane microdomains. In keeping with this, a sizable detergent nonextractable pool of GFP-CL3 was present in the perinuclear Golgi and proximal dendrites in developing hippocampal neurons (see Figure S1A in the Supplemental Data available with this article online, -GODZ arrow and arrowhead; and Figure S1B), and this pool was further increased by coexpression of GODZ (Figure S1A, +GODZ arrow and arrowheads). In immature cortical neurons, a large majority of the CL3 signal that was resistant to detergent treatment was present both in the intracellular perinuclear Golgi-like membranes and in the minor processes (i.e., dendrites) (Figure 2B, upper panel, see line scan in the inset for CL3 signal in the dendrites). Importantly, this detergent-resistant pool of CL3 was almost completely lost when neurons were treated with zaragozic acid, an

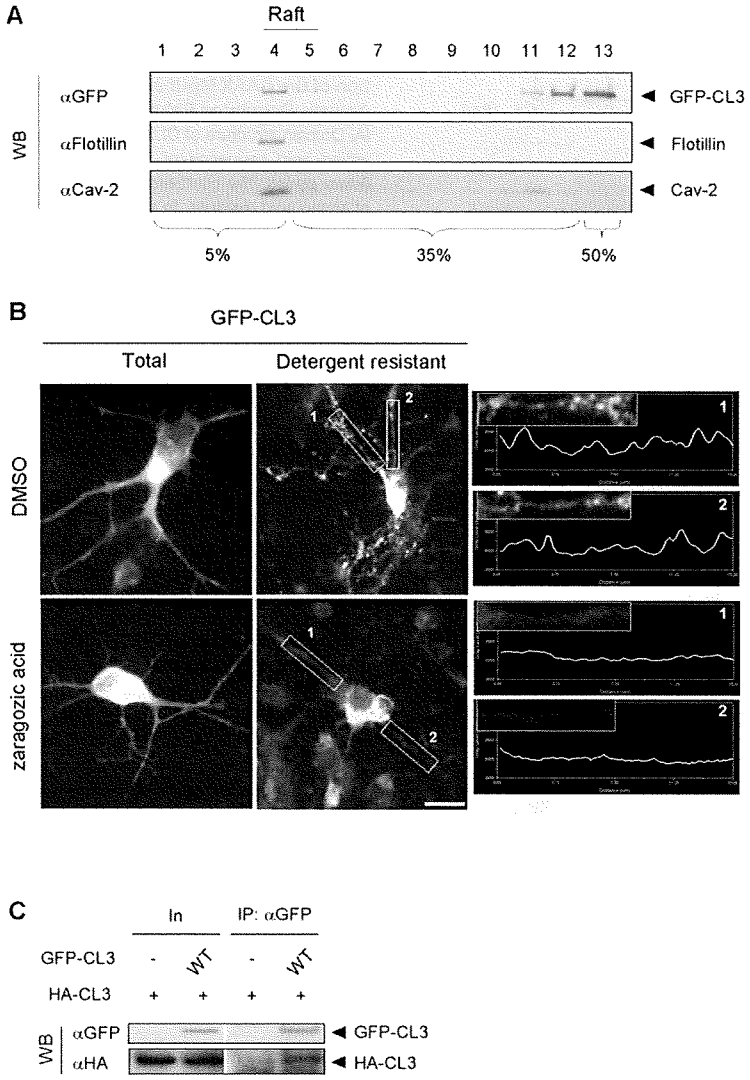

Figure 2. Dendritic Raft Targeting and Multimeric Complex Formation of CL3 in Cortical Neurons

(A) Wild-type GFP-CL3 (WT) expressed in cortical neurons using a synapsin I promoter-driven lentivirus was recovered in the lipid raft fraction (lanes 4–5), as confirmed by the enrichment of raft marker proteins flotillin-1 and caveolin-2 (Cav-2). Fractions 1–4, 5% sucrose; 5–12, 35% sucrose; 13, 50% sucrose.

(B) A sizable portion of total GFP-CL3 fluorescence was recovered after detergent treatment as detergent-resistant GFP-CL3, which was localized in a punctate manner in 2 DIV cortical neurons along the dendrites as well as at the perinuclear region. Dendrites were unambiguously identified as processes of limited length (much shorter than the axon exceeding 100 μm). Line scans of pixel fluorescence, carried out within a chosen field of a 15 μm dendritic segment (in insets 1 and 2) by horizontally tracking the clusters of GFP-CL3, illustrate the spotty presence of raft-inserted CL3 along the dendrites (right panels). Treatment with 100 μM zaragozic acid abolished the dendritic detergent-resistant patches and flattened the line scan profile. Scale bar, 10 μm.

(C) CL3 forms a multimeric complex in cortical neurons. Wild-type CL3 tagged with either HA-tag (HA-CL3) or GFP (GFP-CL3) were coexpressed in cortical neurons by nucleofection and coimmunoprecipitated using an anti-GFP antibody. In, input; IP, immunoprecipitates.

inhibitor of squalene synthase that efficiently depletes membrane cholesterol (Figure 2B, lower panel). These results indicated that CL3 was a genuine component of dendritic lipid rafts and that raft insertion was likely regulated by CL3 prenylation and palmitoylation.

Does CL3 actually share some of the properties known for dendritic raft signaling molecules? A number of raft proteins were previously reported to homo-oligomerize into a multimeric protein complex via lipidification (Zacharias et al., 2002; Huang and El-Husseini, 2005). Indeed, HA-tagged WT CL3 coimmunoprecipitated with GFP-CL3 (Figure 2C) in cortical neurons. Furthermore, a significant fluorescence energy transfer (FRET) was detected between coexpressed CFP-CL3 and YFP-CL3 in live hippocampal neurons, indicative of their genuine molecular proximity in a complex (Figure S2A). Interestingly, Lyn, a well known raft-enriched molecule, colocalized with CL3 in live-untreated, but not in detergent-treated, neurons (Figure S2B). In contrast, the distribution of GluR1, a dendritic protein that is targeted to lipid rafts by palmitoylation (Suzuki et al., 2001; Hering et al. 2003; Hayashi et al. 2005), partially overlapped with CL3 even in detergent-treated neurons (Figure S2C).

CL3 Promotes Dendritogenesis in Cortical Neurons

From previous studies (Takemoto-Kimura et al., 2003; Wayman et al., 2004), it has been speculated that the CaMKK-CaMKI pathway might play a role in the control of neuronal morphology during development. In situ hybridization of embryonic day 17.5 (E17.5) tissues revealed a strong expression of CL3 transcript in the forebrain (Figures 3A and 3B) and in particular in the cortical plate of the cerebral cortex (Figures 3C and 3D). To test whether CL3 was involved in neuronal morphogenesis during this period, either GFP or GFP-CL3 cDNAs were

electroporated into cortical neurons immediately upon dissociation, and the morphology of the neurons was examined 48 hr later, a time point when the majority of neurons under our culture conditions developed well-discernable dendrites and one axon. In control GFP-expressing neurons, little GFP fluorescence overlapped with a Golgi membrane marker, GM130 (Figures 3E and 3F, arrow). In GFP-CL3-overexpressing cortical neurons, however, GFP fluorescence colocalized with GM130 (Figures 3G and 3H, arrow) and also showed discrete enrichment within several dendritic processes (Figures 3G and 3H, arrowhead). Compared to GFP-expressing control neurons (Figure 3I), GFP-CL3-overexpressing neurons appeared to exhibit unaltered axonal extension and branching, while in contrast, increased dendritic growth was found at and in the very vicinity of the soma (Figure 3L). In keeping with this finding, coexpression of mCherry-actin with GFP-CL3 (Figures 3M and 3N), but not with GFP (Figures 3J and 3K), revealed an augmentation of actin-enriched tips at the growing ends (Figures 3M and 3N, arrows) of the nascent processes extending out from the soma, consistent with activation of an actin cytoskeletal remodeling process. To quantify the morphological changes associated with CL3 overexpression, morphometric analyses were performed on the dendrites of GFP-CL3-expressing cortical neurons in a blind fashion. We found that total dendritic length, and in particular the length of the longest dendrite, was most strikingly increased by CL3 overexpression, while the change in branch-tip number remained small and not significant (Figure 3O). CL3-dependent promotion of dendritic growth was detected equally over the whole range of length of primary dendrites (Figure 3P), suggesting that the CL3 effect was unlikely to be restricted to just a subgroup of dendrites, but rather promoted a key common step in early dendritic formation. This CL3-induced effect was not seen with a kinase-inactive K52A mutant (data not shown). Together, these sets of evidence suggested the possibility that CL3 may be involved in early stages of dendritogenesis in developing cortical neurons.

A Required Role of CL3 in Dendritogenesis but Not in Axonogenesis

To critically test this possibility, we next examined the neuronal morphology in neurons where CL3 expression was strongly attenuated by RNA interference, using a short hairpin-type pSUPER vector that also coexpressed a PGK promoter-driven EGFP or mRFP1 gene cassette for morphological tracing. The knockdown efficiency and specificity of the shCL3 vector was prominent enough such that even an overexpressed GFP-CL3 became barely detectable 48 hr after transfection, while the control mRFP1 expression level remained unchanged (Figure 4A). This shCL3 vector was introduced into embryonic cortical neurons by electroporation, and formation of dendrites and axons was studied 48 hr later. While the cortical neurons showed 5–6 dendritic processes in control experiments, shCL3-treated neurons revealed a notable impairment in the number and total length of MAP2-positive dendrites (Figure 4B, arrows). In striking contrast, formation of Tau-1-positive axons was largely spared (Figure 4B, arrowheads). Quantitative morphometric analyses on dendritic or axonal arborizations confirmed that the impairment in shCL3-transfected neurons was actually confined to a selective decline in total dendritic length and in total tip number and did not affect either axonal outgrowth or branching (Figures 4C and 4D). The reduction in dendritic growth was observed throughout the whole range of dendrite length (Figure S3). The striking specificity in dendritic phenotype was also sustained even in shCL3-transfected neurons that were plated following an extensive period (48 hr) of suspension culture that allowed them to maximize the effect of knockdown prior to plating (Figure S4). Knockdown of either CaMKIIα or CaMKIV revealed no phenotype, at least during the very early dendritogenic period that we examined (Figure S5). Taken together, knockdown of CL3 did not interfere with the process of axon specification or axonogenesis, but rather suppressed a subsequent process that was required for dendritogenesis. We next asked whether CL3's kinase activation was a genuine requirement. The abnormality in dendritogenesis could be rescued by additional expression of an shCL3-resistant WT (kinase-active) CL3, but not by that of an shCL3-resistant K52A (kinase-inactive) CL3, demonstrating the absolute necessity of CL3 kinase activity during dendritogenesis (Figure 4E). Consistently, early dendritogenesis, but not axonogenesis, was also impaired in cultured cortical neurons obtained from CL3 null mice (Figure 4F).

In 9 DIV hippocampal neurons, CL3 knockdown diminished total dendritic length and primary dendrite number (Figure S6) and induced an altered Golgi morphology (Figure S7), which was somewhat reminiscent of Golgi vesiculation associated with impaired dendritic polarity (Horton et al., 2005).

A Required Role for CL3 in BDNF-Stimulated Dendritic Growth

We then asked what calcium mobilization might contribute to CL3-dependent stimulation of dendrite development. Brain-derived neurotrophic factor (BDNF) was previously shown to strongly promote dendrite growth and trigger an intracellular calcium rise (e.g., Huang and Reichardt, 2003, for a review). Consistent with published literature, bath application of BDNF induced a slow but clear increase in intracellular Ca^{2+} concentration in the cultured cortical neurons used in our study (Figures 5A–5C). Latencies of onset and oscillatory amplitudes/frequencies varied from neuron to neuron (Figures 5B and 5C). Continuous treatment of cortical neurons with BDNF significantly promoted dendritic growth (Figure 5D, $p < 0.05$, ANOVA with post hoc Tukey-Kramer test). In the presence of a global blocker of CaM kinase activation, KN-93, both constitutive and BDNF-stimulated components of dendritic growth were strongly inhibited

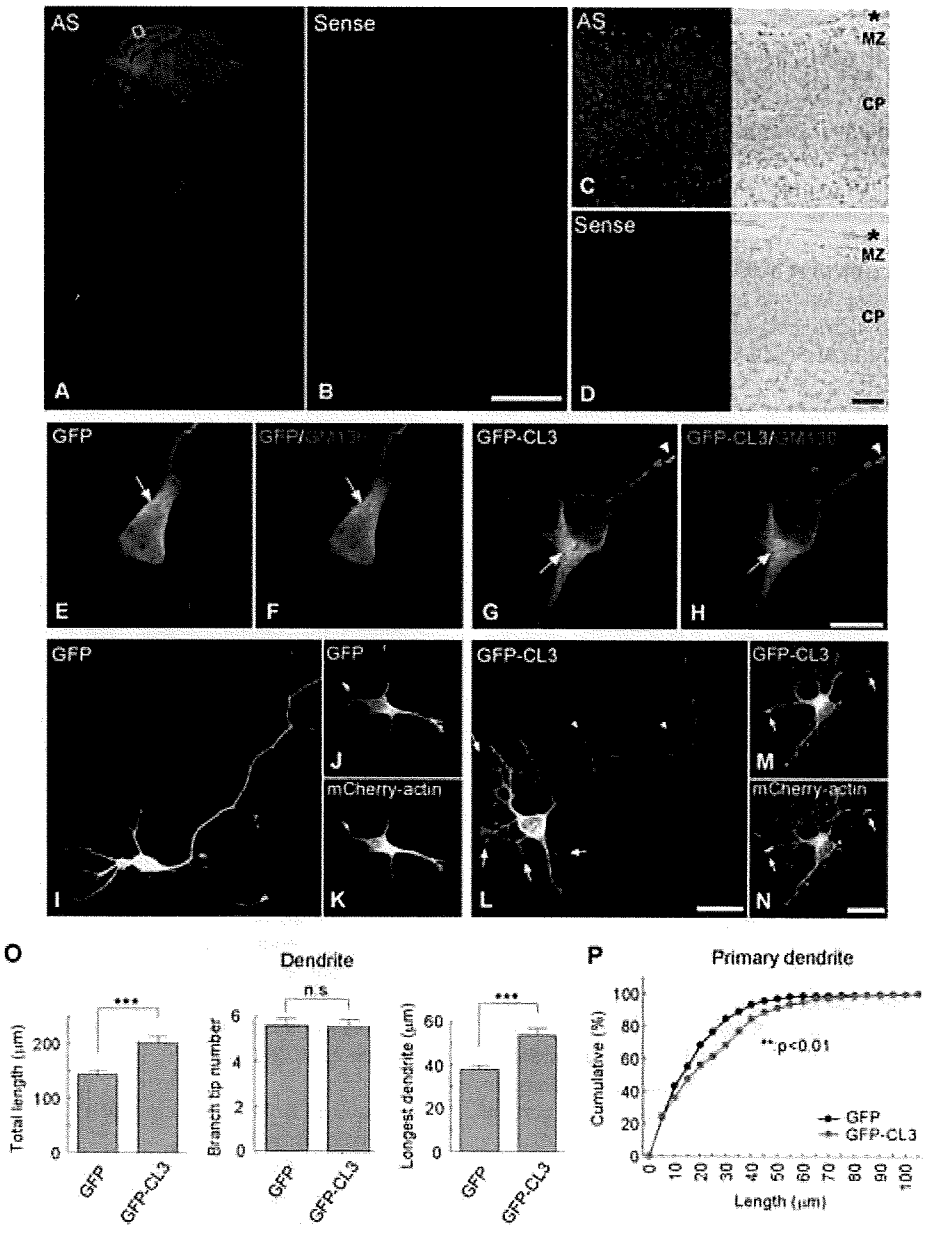

Figure 3. Expression of CL3 in the Developing Cortex and Regulation of Dendritic Morphogenesis in Cultured Cortical Neurons

(A–D) In situ hybridization of mouse embryonic (E17.5) tissue using an antisense (AS) riboprobe revealed an intense signal of CL3 transcript in the developing forebrain. The boxed area of a macroscopic image in (A) is shown at higher magnification (C): (left) hybridized DIG signal only; (right) full-color image (DIG signal in blue-violet + nuclear counterstaining in red). The control sense probe detected little signal (B and D). Asterisk, pia mater; MZ, marginal zone; CP, cortical plate.

(E–H) Membrane localization of CL3 in embryonic cortical cultures. GFP-CL3 distribution detected by anti-GFP immunostaining (G and H) showed colocalization with a Golgi marker, GM130 ([G and H], arrows). GFP-CL3 signals were also enriched within tips of fine dendritic processes ([G and H], arrowheads). Note that the GFP signals in control neurons were separated from the red GM130 immunofluorescence (E and F). Single representative confocal sections are shown.

(I–N) Overexpression of GFP-CL3 facilitated formation of actin-rich thin processes from dendrites and soma. Low-magnification image showed GFP-CL3 signals were distributed both in the nascent dendrites and in the axon ([L], arrow and arrowhead, respectively). In GFP-CL3-expressing neurons, a larger number of thin processes reminiscent of fine dendrites and/or filopodia were present at dendrites and soma ([L and M], arrows), as compared with GFP-expressing neurons (I and J), but not at the axon ([L], arrowheads). These numerous processes contained abundant amounts of β-actin, as shown by enrichment of mCherry-actin (arrows in [N]).

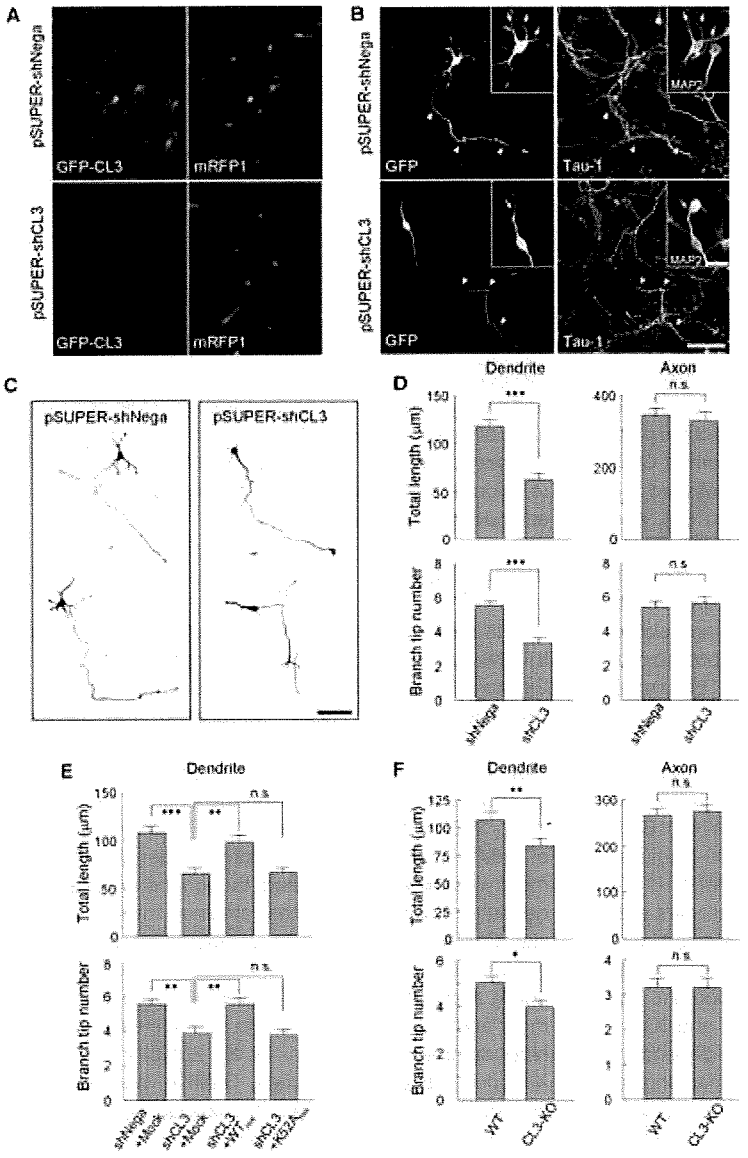

Figure 4. CL3 Loss-of-Function in Embryonic Cortical Neurons Elicits a Specific Impairment in Dendrite Morphogenesis

(A) Efficient downregulation of exogenous GFP-CL3 was achieved by a CL3-targeted shRNA vector (pSUPER-shCL3), but not by a control vector (pSUPER-shNega), in embryonic cortical neurons. The mRFP1 expression, which was driven by a dual promoter in a pSUPER + mRFP1 vector cassette, remained unchanged.

(B) A representative confocal image of an shCL3/GFP-expressing neuron (pSUPER-shCL3) showing impaired dendritogenesis. In this example, an shCL3-expressiong neuron had only a single remaining dendrite (an arrow in the inset), while an shNega-transfected neuron carried 5–6 dendrites (arrows in the inset). On the other hand, no change in axonal morphology was detected (arrowheads). Tau-1 and MAP2 were used to identify axons and dendrites, respectively.

(C) Monochrome diagrams of representative shNega- or shCL3-expressing neurons. The longest process (axon) was unchanged, while the morphology of shorter dendrites near the cell soma was much simplified in shCL3-transfected neurons.

(D) Quantification of morphometric parameters in CL3-knockdown neurons. To quantify, the total length and the dendritic branch tip number were calculated over the dendritic or the axonal arborizations for all branches exceeding 7 μm in length. In shCL3-expressing neurons, both parameters were significantly reduced in the dendrites. On the other hand, neither axonal length nor axonal branch tip number were significantly altered. Number of neurons: shNega, n = 78; shCL3, n = 53. ***p < 0.001; n.s., not significant (p > 0.05) (t test).

(E) Requirement for CL3 kinase activity to rescue shCL3-mediated impairment in dendritogenesis. Introduction of an shCL3-resistant silent mutant of wild-type GFP-CL3 (WT_{res}) successfully rescued the dendritic phenotype elicited by shCL3 on both morphometric parameters. The shCL3-resistant kinase-inactive GFP-CL3 ($K52A_{res}$) was unable to rescue the shCL3 phenotype. Number of neurons: shNega, n = 37; shCL3 + mock, n = 35; shCL3 + WT_{res}, n = 41; shCL3 + $K52A_{res}$, n = 33. **p < 0.01; ***p < 0.001; n.s., not significant (p > 0.05) (ANOVA with post hoc Tukey-Kramer test).

(F) Dendritogenesis, but not axonogenesis, is specifically impaired in cultured cortical neurons from CL3-KO mice. WT, n = 20; CL3-KO, n = 20. *p < 0.05; **p < 0.01; n.s., not significant (p > 0.05) (t test). Scale bars, 50 μm (A–C) and 20 μm ([B], inset).

(Figure 5D). Because KN-93 suppressed dendritic growth to a similar extent under either constitutive or BDNF-stimulated conditions, this raised the possibility of a common involvement of a KN-93-sensitive kinase (Figure 5D). To specifically test this idea, we employed RNAi and measured the degree of suppression of dendritic growth in the absence or presence of BDNF application and found that indeed CL3 knockdown completely phenocopied the effect of KN-93 on dendrites and occluded BDNF-stimulated dendritic growth (Figure 5E).

(O) Facilitation of dendritic outgrowth by CL3 overexpression. Total length, branch tip number, and longest dendrite length are shown. Number of neurons: GFP, n = 30; GFP-CL3, n = 30. ***p < 0.001; n.s., not significant (p > 0.05) (t test).

(P) Cumulative probability analysis shows a significant extension of primary dendrites in GFP-CL3-expressing neurons (**p < 0.01, Kolmogorov-Smirnov test). Numbers of examined dendrites: GFP, n = 258 (from 50 neurons); GFP-CL3, n = 321 (from 50 neurons).

Scale bars, 300 μm (A and B); 50 μm (C and D); 10 μm (E–H); 20 μm (I–N).

Furthermore, dendritic growth was rescued by coexpressing an shCL3-resistant wild-type, but not a membrane anchoring-defective CL3 mutant (Figure 5F). Thus, signaling via membrane-anchored CL3 may play a critical role in BDNF-mediated cortical dendritogenesis during early development.

A Lipid-Raft-Delineated CL3-STEF-Rac Pathway Contributes to the Development of Cortical Dendrites

What are the signaling components that underlie lipidified CL3-mediated dendritic growth? Taking advantage of our finding that CL3 overexpression was accompanied by a sizable increase in the length of primary dendrites (Figures 3O, 3P, and 6A), and in particular its longest dendrite (Figure 3O, right panel; Figure 6B), we next tested the possible contribution of small GTPases downstream of CL3. Coexpression of a dominant-negative Rac abolished the effect of CL3 overexpression (Figures 6A and 6B), and this effect was seen throughout the observed range of primary dendrite length (Figure 6C), supporting the idea that Rac mediated CL3-stimulated dendritic growth. Consistently, we found that CL3 knockdown downregulated Rac activity (Figure 6D). Furthermore, overexpression of a dominant interfering fragment (PHnTSS) of STEF, a specific RacGEF previously implicated in cortical migration and neurite outgrowth (Kawauchi et al., 2003; Matsuo et al., 2002), also potently repressed the CL3 effect (Figures 6A and 6B); however, this effect was less pronounced in dendrites with shorter lengths (<20 μm) (Figure 6C). Both STEF and Rac were detected in the Triton X-100-insoluble low-density membrane fractions enriched for flotillin-1 but devoid of transferrin receptors (Figure 6E), consistent with the presence of a raft-delineated CL3-STEF-Rac pathway. In keeping with this, sustained Rac activity significantly attenuated the impairment in dendrite development observed in CL3-diminished neurons (Figures 6F and 6G).

If raft localization of CL3 was critical for CL3-dependent dendritogenesis, a raft depletion by pharmacological manipulation or a removal of CL3 from rafts by mutation of its palmitoylation sites should significantly perturb dendrite formation and growth. To test this, we pretreated cortical neurons with either mevastatin, an HMG-CoA reductase inhibitor, to deplete membrane cholesterol, and/or with fumonisin B_1, an inhibitor of sphingolipid synthesis. Treatment with either mevastatin or, to a lesser extent, with fumonisin B_1 reduced dendritogenesis (Figures 7A and 7B). A combination of both had no further additive effect (Figures 7A and 7B). As mevastatin was expected to interfere not only with cholesterol synthesis alone but also with protein prenylation, we also examined the effect of zaragozic acid, an inhibitor of squalene synthase, which would disrupt cholesterol synthesis while sparing mevalonate production. Zaragozic acid treatment diminished dendrite formation to a degree similar to the effect seen with mevastatin; a combination of both did not produce a further incremental effect (Figures 7A and 7B). Interestingly, raft depletion by treatment with zaragozic acid abolished the dendritogenic action of overexpressed CL3 (Figure 7C). Together, these results further supported the idea that the presence of intact lipid rafts was critical for CL3 to exhibit its dendritic effect.

In keeping with this, a palmitoylation-site-deficient 4CS mutant of CL3, which was made resistant to shCL3 RNAi vector, was unable to rescue the dendritic effect of CL3 knockdown in cortical neurons (Figure S4C). Intriguingly, in hippocampal neurons, the inaccessibility of 4CS mutant protein toward detergent-resistant raft membranes in CL3-knockdown cells (Figure S8A) was accompanied with the appearance of exuberant thin filopodial processes from the soma (Figure S8B, arrows). These results are consistent with a role of palmitoylation in targeting, and perhaps restricting, CL3 expression to its appropriate sites of cellular actions. Taken together, CL3 palmitoylation may be a useful means to restrict STEF-Rac activation to microdomains in the vicinity of dendritic rafts during early dendritogenesis.

DISCUSSION

Identification of CL3/CaMKIγ as a Privileged Kinase Involved in the Regulation of Dendritic Cytoarchitecture during Early CNS Development

Previous analyses have established the necessity of CaMKII, a predominant form of CaM kinase, as molecular switch required for neuroplasticity in the hippocampus, the barrel cortex, and the visual cortex (Lisman et al., 2002; Fox and Wong, 2005). Furthermore, the role of CaMKII isoforms in several forms of dendritic development was extensively studied, though the exact effect on dendrite morphogenesis has remained rather controversial. CaMKIIα was shown to contribute to dendritic outgrowth in cerebellar granule neurons (Gaudilliere et al., 2004), and CaMKIIβ but not CaMKIIα regulated the movement and branching of filopodia and fine dendrites in rat hippocampal neurons (Fink et al., 2003). In contrast, in *Xenopus* retinotectal neurons, CaMKII was reported to limit dendritic outgrowth and to stabilize dendritic arborization in vivo (Wu and Cline, 1998).

In contrast to CaMKII, which is one of most abundant proteins expressed in the postsynaptic density (PSD) (Kennedy, 2000), CaMKIV in the nucleus plays a critical role in mediating Ca^{2+}-regulated transcription via a CREB/CBP pathway, which is necessary for the formation of long-term synaptic plasticity and long-term memory (Silva et al., 1998; Bito and Takemoto-Kimura, 2003), as well as activity-dependent dendritic elongation (Redmond et al., 2002). In turn, a cytosolic CaMKI activity has been shown to participate in the gating of an ERK/MAP-kinase-dependent form of LTP (Schmitt et al., 2005). Neurite outgrowth was also reported to be regulated by a presumably cytosolic CaMKK-CaMKI/IV pathway: indeed, a constitutively active CaMKIV was suggested to enhance dendritic growth via stabilization of β-catenin (Yu and Malenka, 2003), while a CaMKK inhibitory drug, STO-609, or putative dominant-negative constructs specifically blocking

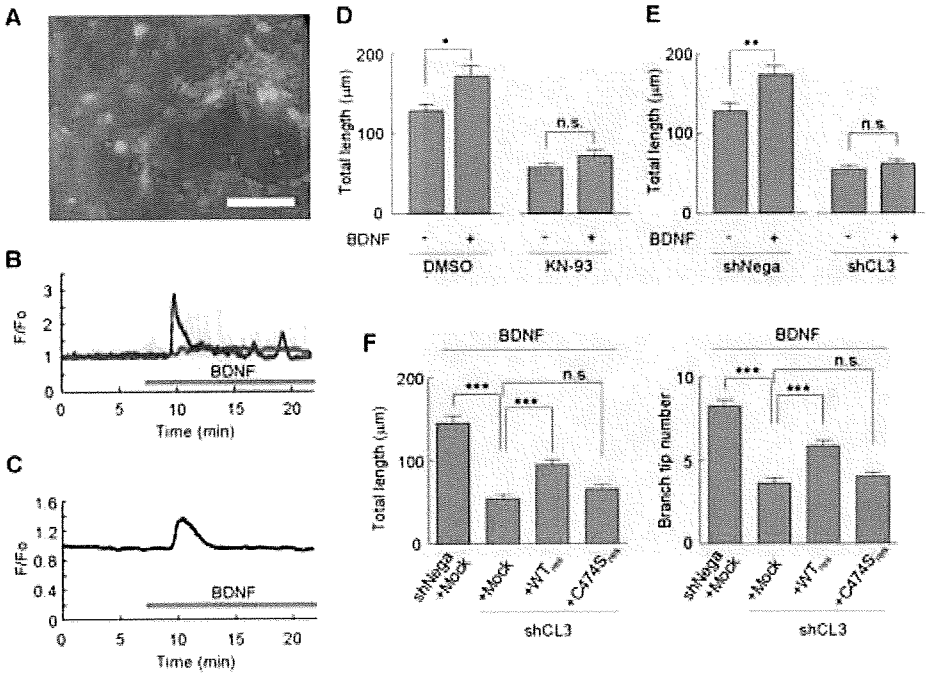

Figure 5. Requirement of CL3 for BDNF-Stimulated Dendrititogenesis

(A) BDNF-induced calcium transients in developing cultured neurons. A representative image of cortical neurons during a typical calcium rise after BDNF bath application is shown in (A). Embryonic cortical neurons (1 DIV) were loaded with a calcium indicator, Fluo-4AM, and calcium responses were measured by time-lapse imaging. A green fluorescence image was overlaid on a DIC image. Colored boxes indicate the location of cells shown in (B). Scale bar, 50 μm.

(B) Representative calcium responses in individual cells after BDNF administration. Three different types of calcium responses were revealed. The majority of cells showed a large transient response followed by smaller repetitive responses (blue), whereas some showed oscillation (yellow) or chronic increases from the baseline (red).

(C) Averaged calcium responses after BDNF administration. An averaged response from 70 cells in a microscopic field is shown.

(D) Cortical neurons were transfected with a morphological tracer, mCherry, and stimulated with BDNF from 6 hr to 48 hr after plating, in the presence or absence of KN-93, a general CaM kinase inhibitor. BDNF treatment maximized dendritogenesis, and this BDNF-stimulated increment was occluded in neurons treated with KN-93. Numbers of neurons: vehicle + DMSO, n = 25; vehicle + KN-93, n = 44; BDNF + DMSO, n = 38; BDNF + KN-93, n = 32.

(E) Quantification of dendritogenesis in BDNF-stimulated CL3-knockdown neurons. CL3 knockdown severely inhibited dendritogenesis induced by BDNF administration, to an extent similar to that obtained with KN-93. Numbers of neurons: vehicle + shNega, n = 40; vehicle + shCL3, n = 41; BDNF + shNega, n = 40; BDNF + shCL3, n = 40.

(F) Suppression by CL3 knockdown of BDNF-stimulated dendritogenesis can be rescued by coexpression of an shRNA-resistant wild-type CL3 (WTres), but not by a nonlipidified mutant CL3 (C474Sres). Numbers of neurons: shNega + mock, n = 52; shCL3 + mock, n = 57; shCL3 + WTres, n = 57; shCL3 + C474Sres, n = 55.

***p < 0.001; n.s., not significant (ANOVA with post hoc Tukey-Kramer test).

either CaMKK or cytosolic CaMKI/CaMKIV (but not nuclear CaMKIV) activities prevented axonal extension and growth cone dynamics as well as neurite extension (Schmitt et al., 2004; Wayman et al., 2004).

Taken together, multiple CaM kinase pathways that are segregated in distinct subcellular compartments may regulate several critical steps converging onto dendrite elongation and maturation. This prompted us to investigate the particular role of CL3/CaMKIγ (Takemoto-Kimura et al., 2003; Nishimura et al., 2003), a membrane-anchored form of CaMKI, which was highly expressed in the cortical plate neurons of the mouse embryo (this study). Intriguingly, we found a specific impairment in the number and total lengths of dendrites in CL3 knockdown and CL3 null neurons (Figure 4 and Figure S3), while axonal morphology was not significantly distinct from controls. Knockdown of CL3 prior to plating of neurons strengthened this suppressive effect on the dendrites while still sparing the axons (Figure S4). Taken together, our data suggested a prominent role of CL3 during the early stages of dendritogenesis that presumably followed completion of the axon/dendrite specification.

While this paper was under review, an independent study reported that CL3/CaMKIγ may regulate activity-dependent dendritic growth at an even later stage of development in hippocampal neurons (Wayman et al., 2006; see also Figures S6 and S7 of this study).

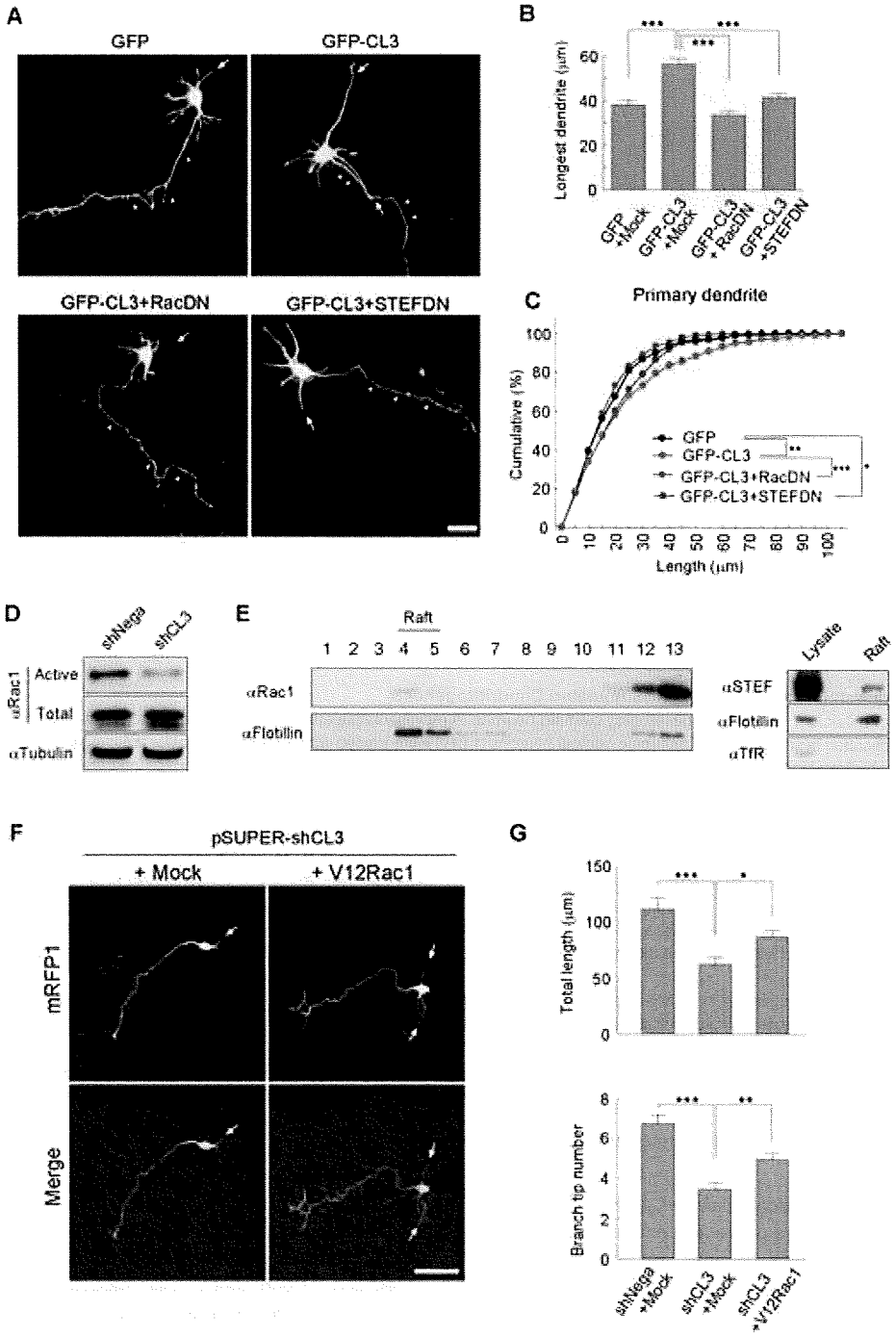

Figure 6. A Critical Role for RacGEF STEF and Rac in Mediating CL3-Induced Dendritic Outgrowth

(A) Cortical neurons were cotransfected with GFP-CL3 and either dominant-negative Rac1 (RacDN) or dominant-interfering fragment of STEF (STEFDN) together with a morphometric tracer, mRFP1. Examples for dendrites (arrows) and axons (arrowheads) are shown. Scale bar, 20 μm.

(B) Quantification of longest dendrite. Number of neurons: GFP + mock, n = 51; GFP-CL3 + mock, n = 50; GFP-CL3 + RacDN, n = 57; GFP-CL3 + STEFDN, n = 60. ***p < 0.001 (ANOVA with post hoc Tukey-Kramer test).

(C) Cumulative probability analysis of the length of primary dendrites showed that inhibition of STEF and Rac activity suppressed the extension of primary dendrites induced in GFP-CL3-expressing neurons. Number of examined dendrites (neurons): GFP, n = 324 (from 51 neurons); GFP-CL3, n = 332 (from 50 neurons); GFP-CL3 + RacDN, n = 328 (from 57 neurons); GFP-CL3 + STEFDN, n = 378 (from 60 neurons). *p < 0.05; **p < 0.01; ***p < 0.001 (Kolmogorov-Smirnov test).

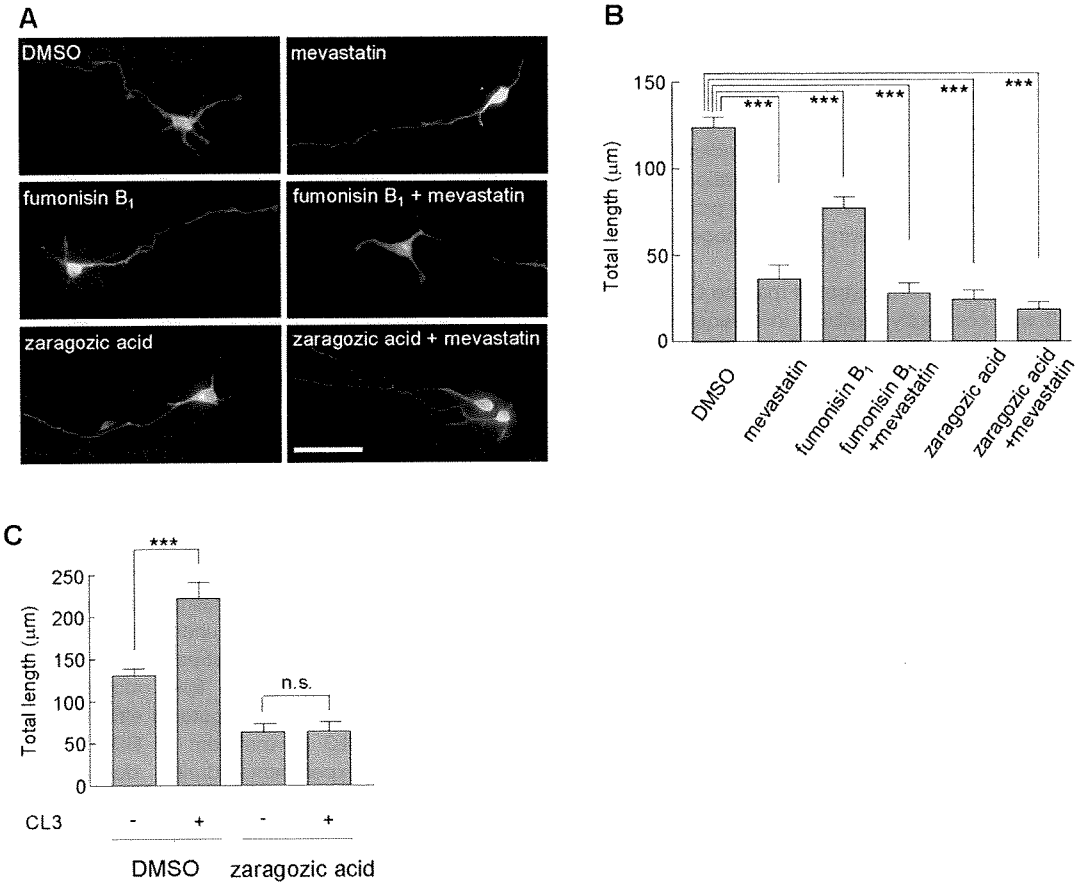

Figure 7. Raft Depletion Abolishes CL3-Mediated Dendrite Outgrowth

(A) Cortical neurons were transfected with a morphological tracer, mCherry, and cultured in the presence of various combinations of raft-depleting agents from 6 hr to 48 hr after plating. Disruption of cholesterol/sphingolipid synthesis strongly inhibited formation and outgrowth of the dendritic processes around the soma. Scale bar, 50 μm.

(B) Ensemble average of experiments shown in (A). DMSO, n = 10; 10 μM mevastatin, n = 15; 10 μM fumonisin B_1, n = 15; 10 μM fumonisin B_1 and 10 μM mevastatin, n = 15; 100 μM zaragozic acid, n = 15; 100 μM zaragozic acid and 10 μM mevastatin, n = 15. ***p < 0.001 (ANOVA with post hoc Tukey-Kramer test).

(C) Raft depletion using zaragozic acid abolished the increase of dendritogenesis induced by CL3 overexpression. A significant CL3-mediated increase in dendritic growth was shown in the DMSO control, but this significant increase was abolished by raft depletion in the presence of zaragozic acid (two-way ANOVA, CL3 effect, $F_{1,65} = 8.65$, $p = 0.0045$; drug effect, $F_{1,65} = 51.95$, $p < 0.0001$; CL3 × drug, $F_{1,65} = 8.38$, $p = 0.0052$). ***p < 0.001 (post hoc Bonferroni test). DMSO, n = 15 (−CL3), n = 24 (+CL3), 100 μM zaragozic acid, n = 15 (−CL3), n = 15 (+CL3).

Control of CL3 Targeting to Lipid Microdomains by a Kinase-Activity-Regulated Dual Lipidification Mechanism

In polarized neural cells, covalently attached lipid modification of proteins is important for membrane targeting and expression of proper function in the vicinity of specialized membrane compartments. Largely based on quantitative work on Ras and PSD-95, a palmitoylation/depalmitoylation cycle has been previously suggested to play a crucial regulatory role in determining the proper

(D) The amount of GTP-bound active Rac1 was measured by a Pak1-PBD pulldown assay using cortical neurons transfected with shNega or shCL3 vector. The amount of active Rac1 was reduced by CL3 knockdown.

(E) Presence of Rac1 and STEF immunoreactivities in lipid raft fractions of cortical neurons. For STEF detection, a pooled and concentrated raft fraction was used. Transferrin receptor was used as a non-raft membrane marker.

(F) Representative images of shCL3/mRFP1-expressing neurons coexpressing constitutively active GFP-Rac1 (+V12Rac1) or GFP (+mock). Expression of constitutively-active GFP-Rac1 (+V12Rac1) restored appearance of multiple dendrites (arrows) in shCL3-expressing neurons, while expression of GFP alone did not. Scale bar, 50 μm.

(G) Quantification of dendritic morphogenesis confirmed that constitutively active GFP-Rac1 attenuated the specific impairment of dendritic morphology induced by shCL3 transfection. Number of neurons: shNega + mock, n = 22; shCL3 + mock, n = 47; shCL3 + V12Rac1, n = 49. *p < 0.05; **p < 0.01; ***p < 0.001 (ANOVA with post hoc Tukey-Kramer test).

trafficking and function of palmitoylated signaling proteins (Huang and El-Husseini, 2005). Dynamic regulation of palmitoylation was already shown for a large number of synaptic constituents such as AMPA-receptor subunits (Hayashi et al., 2005), GABAR γ-subunits (Keller et al., 2004), and GRIP/ABP (DeSouza et al., 2002), indicating a critical role for neuronal PAT in synaptic maturation and maintenance. However, a direct involvement of protein palmitoylation in early stages of neuronal morphogenesis has not been examined.

In this work, we demonstrated that the C-terminal end of CL3 was covalently modified in a sequential manner by prenylation and by palmitoylation. A dually lipidified CL3 was generated in a kinase-activity-dependent manner, in part via the PAT GODZ (Uemura et al., 2002), resulting in an efficient enrichment into dendritic-raft-like lipid microdomains.

We then found that dually lipidified CL3 was likely to be partitioned and targeted to close proximity of dendritic lipid microdomains. Consistently, CL3 showed self-association (Figure 2C and Figure S2A), a property that is not unusual for palmitoylated or dually lipidified proteins (Zacharias et al., 2002). However, we failed to detect any Ca^{2+}/CaM-independent kinase activity of CL3, even under conditions where CL3 multimerization was present. This is distinct from the property of CaMKII, in which dodecamerization was shown to promote a Ca^{2+}/CaM-independent kinase activity that outlasted the duration of the incoming Ca^{2+} mobilization through an autophosphorylation mechanism. We thus speculate that oligomerization, if any, of prenyl-/palmitoyl-CL3 may have roles other than the generation of an autonomous kinase activity, such as sustaining a high degree of molecular proximity and concentration that favors signal amplification and increases the specificity and efficiency of coupling to downstream signaling events.

A BDNF-CL3-Rac Pathway May Underlie Excitation-Morphogenesis Coupling during Early Cortical Dendritogenesis

Previously, neuronal activity has been shown to promote initiation of dendrite formation via small GTPases such as Rac and Cdc42 (Luo, 2002; Van Aelst and Cline, 2004). To date, however, knowledge about how neuronal activity regulates these small GTPases is still limited. The strongest evidence in favor of activity-induced dendritic arborization so far involved several Ca^{2+}-regulated transcriptional factor such as CREB, NeuroD, and CREST (Gaudilliere et al., 2004; Konur and Ghosh, 2005), though the cellular mechanisms linking nuclear events and neuronal morphogenesis remained as yet largely undetermined. Here we found that a membrane-bound CaM kinase, CL3/CaMKIγ, may possibly act downstream of BDNF and Ca^{2+} signals to promote dendritic cytoskeletal remodeling via the small GTPase Rac, especially during early stages of dendritic development. Furthermore, we provided several lines of evidence that collectively indicated that CL3-STEF-Rac signaling triggered at or in the vicinity of lipid rafts may play a critical role.

Could lipid rafts, also known as sphingolipid- and cholesterol-rich membrane microdomains, be distributed in an asymmetric fashion such that some of these may influence dendrite targeting of signaling proteins such as CL3? In support for such an idea, depletion of cellular cholesterol/sphingolipid content in cultured neurons revealed an important role for cholesterol (Fan et al., 2002) or sphingolipids (Schwarz and Futerman, 1998; Pelled et al., 2003) in dendritic growth and spine maintenance (Hering et al., 2003). In addition, no responsiveness to glutamate application was reported in neonatal cortical neurons of a mutant mouse deficient in cholesterol biosynthesis, despite a normal amount of GluR and NMDAR subunit expression, indicating a possible defect in membrane insertion of dendritic glutamate receptors (Wassif et al., 2001). A distinct kind of raft-mediated asymmetry may play a role in axonal fate specification (Da Silva et al., 2005).

If raft formation was coupled with the creation of a polarized asymmetry of signaling molecule distribution, how could this possibly underlie a morphogenetic response, especially downstream of BDNF? Recruitment of activated TrkB to lipid rafts (Suzuki et al., 2004) could evidently contribute to efficient coupling to raft-targeted CL3 downstream of BDNF. In neurons, fractionation experiments during development have also previously revealed a privileged association of Rac with rafts, but not of RhoA or Cdc42 (Kumanogoh et al., 2001; see also Figure 6E). We additionally found that a portion of STEF was clearly present in the raft fractions as well (Figure 6E). As the fragment encompassing the PHnTSS domain of STEF (PHnTSS) has been shown to act as a specific dominant-negative form for both STEF and Tiam1 (Matsuo et al., 2002), it remains possible that there may also be an additional contribution of Tiam1, a known substrate for CaMK activity (Tolias et al., 2005).

Taken together, dual lipidification of CL3 may be an efficient mechanism not only to target it into rafts and to limit its protein diffusion parallel to the lipid bilayer, but also to generate a membrane-delimited area of Rac activation within segregated dendritic lipid microdomains at the vicinity of Ca^{2+}-mobilization events. Further studies are needed to substantiate such a hypothesis.

In conclusion, we here uncovered a novel role for CL3/CaMKIγ in the regulation of Rac-dependent dendritic cytoskeletal reorganization, and we found evidence for CL3 in mediating BDNF-stimulated dendritic growth. Through a dual and sequential lipidification mechanism, the unique C-terminal region of CL3 was covalently lipid-modified in a kinase-activity-dependent manner, leading to a privileged partition of membrane-anchored CL3 into dendritic-raft-like lipid microdomains. This membrane-sorting mechanism, unprecedented for a neuronal Ser/Thr kinase, in turn may efficiently localize Rac activity and thereby regulate dendritogenesis. Thus, CL3 turned

out to represent a key element in the Ca^{2+}-dependent and lipid-raft-delineated switch that turned on activity-regulated dendrite formation in developing cortical neurons.

EXPERIMENTAL PROCEDURES

Cloning and Plasmid Constructions

A detailed description of all plasmids can be found in the Supplemental Data.

Immunocytochemistry

Cells were fixed in 4% paraformaldehyde/4% sucrose/phosphate-buffered saline (PBS) (−) at room temperature for 20 min, and immunostaining was carried out as described (Takemoto-Kimura et al., 2003). Additional methods can be found in the Supplemental Data.

Western Blot Analysis

For western blot analysis, primary antibodies were as follows: rat anti-GFP (Nacalai Tesque, Japan), rat anti-HA (Roche Diagnostics), mouse anti-Flotillin-1, mouse anti-Caveolin-2, and anti-Rac1 (BD Transduction Laboratories). A rabbit anti-STEF antibody was as described (Matsuo et al., 2002). Chemiluminescence detection was performed using HRP-conjugated anti-rat and anti-mouse IgG and ECL-Plus reagent (Amersham Biosciences).

Metabolic Labeling and Coimmunoprecipitation

For metabolic labeling, COS-7 cells plated onto 6-well plates were transfected with wild-type and mutant GFP-CL3 vectors using Fugene6 reagent (Roche Diagnostics). For mevalonate labeling, a pMev vector (ATCC), which encoded a transporter that augmented mevalonic acid uptake, was cotransfected with GFP-CL3 for 24 hr. Cells were pretreated with 40 μM Compactin (Wako, Japan) for 2 hr, then incubated for 20 hr in growth medium supplemented with 40 μM Compactin and 0.1 mCi/ml of [^{3}H]-mevalonolactone (PerkinElmer or ARC). Palmitate labeling was initiated 48 hr after transfection by pretreating cells with serum-free medium (DMEM with 1% fatty-acid-free bovine serum albumin [Sigma]) for 1 hr, and then incubating for an additional 3 hr in the serum-free medium supplemented with 0.4 mCi/ml of [^{3}H]-palmitic acid (PerkinElmer). After metabolic labeling, cells were washed twice in ice-cold phosphate-buffered saline (PBS) (−) and lysed in lysis buffer containing 50 mM Tris-HCl (pH 7.5), 100 mM NaCl, 2 mM $MgCl_2$, 10% glycerol, 1% Triton X-100, and a Complete protease inhibitor cocktail (Roche Diagnostics). Lysates were immunoprecipitated using a rabbit anti-GFP polyclonal antibody (Molecular Probes) and Protein-A-Sepharose (Amersham Biosciences). Immunoprecipitates were washed three times in lysis buffer and boiled in 4× Laemmli buffer containing 5 mM DTT for 3 min and were subjected to SDS-PAGE. Incorporated mevalonolactone and palmitic acid were digitally detected using a BAS-5000 bioimage analyzer and quantified using Multi Gauge software (Fujifilm, Japan).

In coimmunoprecipitation assays, cortical neurons were transfected with GFP-CL3 and HA-CL3 vectors by electroporation using Nucleofector (Amaxa Biosystems) and plated onto poly-D-Lysine-coated 6 cm dishes at the density of 4 × 10^5/cm^2 and then harvested at 2 DIV. Immunoprecipitation was performed as described above.

Lentivirus Production, Infection, and Lipid Raft Fractionation

A 536 bp synapsin I promoter was isolated by PCR from rat genomic DNA and inserted into CS-CA-MCS (Miyoshi et al., 1998) to replace the original chicken actin promoter. EGFP-CL3 fragment was further inserted and cotransfected with pCAG-HIVgp and pCMV-VSV-G-RSV-Rev into HEK293T cells using Fugene6 reagent to generate a self-inactivating lentivirus vector. All original lentivirus vectors were provided by Dr. Hiroyuki Miyoshi (RIKEN-BRC, Japan). Concentrated virus solutions were obtained by ultracentrifugation at 80,000 × g, and virus titer was determined using HeLa cells. Cortical neurons (1 DIV) were infected with lentivirus for 5 hr at a nominal MOI of about 0.2, and after washout, maintained in Neurobasal containing 0.5 mM Glutamax, 1 × B27, and 25 μg/ml insulin. Under these conditions, GFP-positive glial cells (as determined by GFAP expression) were less than 6%. Though the nominal MOI was about 0.2, this is very likely to be an underestimate, as it was calculated based on the induction of trace EGFP fluorescence in heterologous cells. Lipid raft preparations were performed 2 days after infection (3 DIV).

Lentivirus-infected cortical neurons in 10 cm dishes (3.5 × 10^5 cells/cm^2) were harvested at 3 DIV for preparation of detergent-insoluble membrane fractions according to Suzuki et al. (2004) with minor modifications. Thirteen fractions (1 ml each) were collected and 15 μl of each fraction were subjected to SDS-PAGE followed by western blot analysis. To obtain a concentrate of the raft fractions in Figure 5E, raft fractions (fractions 4 and 5) were pooled, and a portion of it (1.4 ml) was ultracentrifuged at 20,000 × g for 1 hr at 4°C. The pellet was resuspended in 140 μl of Buffer A (50 mM Tris-HCl [pH 7.5], 50 mM NaCl), and 15 μl of the final sample was subjected to SDS-PAGE and western blot analysis.

Cell Culture Preparation and Visualization of Raft-Targeted Proteins

COS-7 cells were maintained in Dulbecco's modified Eagle medium (DMEM) containing 10% heat-inactivated fetal calf serum (FCS). Dissociated cortical cultures from embryonic day 19 Sprague-Dawley rats were prepared as described previously for rat hippocampal cultures (Bito et al., 1996) with minor modifications. Cortical neurons were plated onto 12 mm poly-L-Lysine-coated coverslips at the density of 5 × 10^5 cells per coverslip in a 24-well plate.

Gene targeting of CL3/CaMKIγ was carried out in a C57BL/6-derived ES cell line RENKA (Mishina and Sakimura, 2007) by insertional mutagenesis. The exons 2 and 3 of mouse the *Camk1g* gene, which contained the kinase ATP-binding site, were deleted and replaced by a targeting construst such that the first methionine of CL3 was fused in-frame to an hCrePR-IRES-EGFP cassette that was juxtaposed to an inverted neomycin resistance gene flanked by FRT sites. A detailed analysis of the CL3/CaMKIγ null mouse mutant will be described elsewhere (S.T.-K., M.O., T. Takeuchi, K. Sakimura, M.M., H.O., and H.B, unpublished data). Cortical mouse cultures were prepared from embryonic day 17 C57BL/6J wild-type or CL3 null mice.

For visualization of in situ raft-targeted GFP-fusion proteins, rat cortical or mouse hippocampal neurons were washed with KRH buffer (Suzuki et al., 2004) containing 2 mM Ca^{2+} on ice, permeabilized with 0.1% Triton X-100/KRH(+) for 2 min on ice, washed gently, and then fixed. Raft depletion in cortical neurons was carried out by including one of the following drugs (10 μM mevastatin, 10 μM fumonisin B_1, 10 μM fumonisin B_1 and 10 μM mevastatin, 100 μM zaragozic acid, 100 μM zaragozic acid, and 10 μM mevastatin) in the culture medium from 6 hr after plating onward for an additional 42 hr. mRFP1 was nucleofected for accurate visualization of the contours of individual neurons.

In one instance, rat hippocampal neurons obtained from P0–1 Sprague-Dawley rats (Bito et al., 1996) were used to quantify FRET between CL3 molecules (Figure S2A).

Morphometric Analysis of the CL3-Associated Phenotype in Cultured Neurons

Dissociated cortical cultures from embryonic day 19 Sprague-Dawley rats were prepared as described previously for rat or mouse hippocampal cultures (Bito et al., 1996; Furuyashiki et al. 2002) with minor modifications. Cortical neurons were transfected immediately after dissociation by electroporation using Nucleofector and plated onto 12 mm poly-L-Lysine-coated coverslips at the density of 5 × 10^5 cells per coverslip (rats) or 7.5 × 10^5 cells per coverslip (mice) in 24-well plates, and then fixed at 2 DIV. Presumably because of a relatively low amount of plasmid transfer across neuronal membranes during electroporation procedure, use of a strong CAG promoter-driven expression cassette was needed to reliably express foreign genes.

Further, to unequivocally ascertain the phenotypes of neurons expressing various shRNA vectors and rescue constructs, we carried out all quantitative analyses based upon immunostaining of the morphometric markers, either GFP or mRFP1 (a kind gift from Dr. Roger Y. Tsien, HHMI, UCSD). This allowed us to obtain clearer images of neuronal contours, thus facilitating morphometric analyses. The transfection efficiency was relatively high (about 50% in our hands using this protocol) when examined within a day after electroporation. Thus, we were able to improve the accuracy of visualization in all morphometric experiments by simply mixing the transfected cells with nontransfected cells prepared in parallel, at a ratio of 1:20 (rats) or 1:10 (mice), before plating. Dendritic and axonal arborizations of most transfected neurons could then be traced in total isolation while they still formed a dense network with neighboring untransfected neurons. Neurons expressing pSUPER-type vectors revealed negligible amounts of either cell death (0%–0.5%) as measured by TUNEL staining (Roche Diagnostics) or dsRNA-induced interferon-like response monitored using a muMx2 promoter-luc vector (a kind gift from Dr. Atsushi Asano, Hokkaido University) (Alvarez et al., 2006).

In the Rac1-rescue experiments, even an intermediate-level expression of a constitutively active Rac mutant, GFP-V12Rac1, using a CAG promoter usually resulted in an aberrant neuronal morphology, such as exuberant lamellipodia formation at the cell soma and premature detachment from the glass coverslip. To circumvent this problem, GFP-V12Rac1 was introduced using a CMV promoter-based plasmid vector, as the observed expression level was lower than that obtained using a CAG promoter vector. A few neurons still showed an aberrant somata size and shape and thus were excluded from analyses.

Images of neuronal morphologies were captured based on immunoreactivities against GFP or mRFP1, using the Olympus BX51 microscopy system with the 20× objective or 40× objective in the cases of CL3-overexpression experiments to visualize fine protrusions for cumulative probability analysis. Dendrites and axons were identified by standard morphological criteria. As the majority of neurons, in our cortical culture preparation, possessed only one clearly classifiable axon and one or more dendrites, neurons with nonpyramidal morphological features (such as multiple axons or no classifiable processes) were excluded from analyses. The total length and the dendritic branch tip number were determined manually using NeuronJ 1.1.0 (Meijering et al., 2004), plug-in software for ImageJ (NIH). Representative images were acquired using the LSM 510META confocal microscope with the 40× objective. All analyses were performed by an observer blinded to the identity of the transfected constructs.

In experiments described in Figure S4, electroporated neurons were initially cultured as a suspension in a growth medium, without plating, in plastic centrifuge tubes at the density of 2×10^6 cells/ml, while neurons were allowed to form aggregation. Forty-eight hours later, aggregated neurons were then dissociated mechanically by gentle pipetting and plated onto 12 mm poly-L-Lysine-coated coverslips at the density of 1×10^6 cells per coverslip. Fixation and analysis were carried out 24 hr later.

Mouse hippocampal neurons were transfected using Lipofectamine 2000 (Invitrogen) at 7 DIV and analyzed at 9 DIV. Morphometric analyses of hippocampal neurons were performed as essentially described above for cortical neurons. Only primary dendrites were traced using ImageJ/NeuronJ software.

In Situ Hybridization

In situ hybridization using DIG technology (Roche Diagnostics) was performed essentially as described (Ohmae et al., 2006). For the generation of antisense and sense cRNA probes, a 374 bp fragment corresponding to the nucleotide position 964–1337 of CL3 was subcloned into pBluescriptII KS+ vector (Stratagene).

BDNF Application and Calcium Imaging in Cortical Neurons

BDNF (generously provided by Dainippon Sumitomo Pharma, Osaka, Japan, by courtesy of Dr. Chikao Nakayama) and/or KN-93 (Calbiochem) were added to cells at 6 hr after plating at the final concentration of 50 ng/ml and 10 μM, respectively. Bath application was performed by dissolving the reagents in one-half volume of the conditioned culture medium and by mixing this gently with the remaining half of the original medium in the dish. No medium change was done thereafter till fixation.

Fluorescent calcium imaging was performed essentially as described previously (Furuyashiki et al., 2002). A detailed description of further experimental conditions can be found in the Supplemental Data.

Rac1 Pull-Down Assays, Measurement of Fluorescence Resonance Energy Transfer, and Quantification of Golgi Deformation

A detailed description of experimental procedures can be found in the Supplemental Data.

Statistical Analysis

Statistical analyses were performed using Prism 4.0 (GraphPad Software) and JMP5.1.2 (SAS Institute). Student's t test was used for comparisons of two groups. One- or two-way analysis of variance (ANOVA) with post hoc Tukey-Kramer or Bonferroni test was used for factorial analysis between more than three groups. The Kolmogorov-Smirnov test was applied to verify whether the bidirectional effect of CL3 manipulation occurred throughout all dendrites or was restricted to a subpopulation. All data are shown as mean ± standard error of means (SEM), unless otherwise mentioned.

Supplemental Data

The Supplemental Data for this article can be found online at http://www.neuron.org/cgi/content/full/54/5/755/DC1/.

ACKNOWLEDGMENTS

We thank A. Asano, Z. Honda, Y. Ihara, A. Miyawaki, H. Miyoshi, S. Narumiya, F. Oyama, B. Sabatini, and R.Y. Tsien for providing plasmids; S. Wada, M. Morishima-Kawashima, and Y. Ihara for a raft fractionation protocol; T. Furuyashiki for generating EGFP-GluR1; K. Ohkubo for assistance with in situ hybridization; and all members of the Bito laboratory for discussion. We acknowledge the invaluable support of H. Mori in designing a successful targeting vector and of T. Takeuchi and K. Sakimura for an ongoing collaboration to generate and characterize CL3 null mice. We are also indebted to assistance from K. Saiki, Y. Kondo, and T. Kinbara. This work was supported in part by Grants-in-Aid from the MEXT and MHLW of Japan, by a JST-SORST investigatorship, and by awards from the Astellas Foundation for Research on Metabolic Disorders, the Brain Science Foundation, the Cell Science Research Foundation, the Japan Foundation for Applied Enzymology, the Kowa Life Science Foundation, the Novartis Foundation (Japan) for the Promotion of Science, the Shimadzu Science Foundation, the Takeda Foundation, the Toray Science Foundation, and the Human Frontier Science Program. N.A.-I. and H.F. are predoctoral fellows, and M.N. is a postdoctoral fellow from the Japan Society for the Promotion of Science.

Received: May 23, 2006
Revised: December 30, 2006
Accepted: May 16, 2007
Published: June 6, 2007

REFERENCES

Alvarez, V.A., Ridenour, D.A., and Sabatini, B.L. (2006). Retraction of synapses and dendritic spines induced by off-target effects of RNA interference. J. Neurosci. *26*, 7820–7825.

Anderson, R.G.W., and Jacobson, K. (2002). A role for lipid shells in targeting proteins to caveolae, rafts, and other lipid domains. Science *296*, 1821–1825.

Bito, H., and Takemoto-Kimura, S. (2003). Ca^{2+}/CREB/CBP-dependent gene regulation: a shared mechanism critical in long-term synaptic plasticity and neuronal survival. Cell Calcium *34*, 425–430.

Bito, H., Deisseroth, K., and Tsien, R.W. (1996). CREB phosphorylation and dephosphorylation: a Ca^{2+}- and stimulus duration-dependent switch for hippocampal gene expression. Cell *87*, 1203–1214.

Ciani, L., and Salinas, P.C. (2005). WNTs in the vertebrate nervous system: from patterning to neuronal connectivity. Nat. Rev. Neurosci. *6*, 351–362.

Cline, H.T. (2001). Dendritic arbor development and synaptogenesis. Curr. Opin. Neurobiol. *11*, 118–126.

Da Silva, J.S., Hasegawa, T., Miyagi, T., Dotti, C.G., and Abad-Rodriguez, J. (2005). Asymmetric membrane ganglioside sialidase activity specifies axonal fate. Nat. Neurosci. *8*, 606–615.

DeSouza, S., Fu, J., States, B.A., and Ziff, E.B. (2002). Differential palmitoylation directs the AMPA receptor-binding protein ABP to spines or to intracellular clusters. J. Neurosci. *22*, 3493–3503.

El-Husseini, A.E.-D., and Bredt, D.S. (2002). Protein palmitoylation: a regulator of neuronal development and function. Nat. Rev. Neurosci. *3*, 791–802.

Fan, Q.W., Yu, W., Gong, J.S., Zou, K., Sawamura, N., Senda, T., Yanagisawa, K., and Michikawa, M. (2002). Cholesterol-dependent modulation of dendrite outgrowth and microtubule stability in cultured neurons. J. Neurochem. *80*, 178–190.

Fink, C.C., Bayer, K.-U., Myers, J.W., Ferrell, J.J.E., Schulman, H., and Meyer, T. (2003). Selective regulation of neurite extension and synapse formation by the β- but not the α-isoform of CaMKII. Neuron *39*, 283–297.

Fox, K., and Wong, R.O. (2005). A comparison of experience-dependent plasticity in the visual and somatosensory systems. Neuron *48*, 465–477.

Fukata, M., Fukata, Y., Adesnik, H., Nicoll, R.A., and Bredt, D.S. (2004). Identification of PSD-95 palmitoylating enzymes. Neuron *44*, 987–996.

Furuyashiki, T., Arakawa, Y., Takemoto-Kimura, S., Bito, H., and Narumiya, S. (2002). Multiple spatiotemporal modes of actin reorganization by NMDA receptors and voltage-gated Ca^{2+} channels. Proc. Natl. Acad. Sci. USA *99*, 14458–14463.

Gaudilliere, B., Konishi, Y., de la Iglesia, N., Yao, G., and Bonni, A. (2004). A CaMKII-NeuroD signaling pathway specifies dendritic morphogenesis. Neuron *41*, 229–241.

Hayashi, T., Rumbaugh, G., and Huganir, R.L. (2005). Differential regulation of AMPA receptor subunit trafficking by palmitoylation of two distinct sites. Neuron *47*, 709–723.

Hering, H., Lin, C.C., and Sheng, M. (2003). Lipid rafts in the maintenance of synapses, dendritic spines, and surface AMPA receptor stability. J. Neurosci. *23*, 3262–3271.

Higgins, D., Burack, M., Lein, P., and Banker, G. (1997). Mechanisms of neuronal polarity. Curr. Opin. Neurobiol. *7*, 599–604.

Hook, S.S., and Means, A.R. (2001). Ca^{2+}/CaM-dependent kinases: from activation to function. Annu. Rev. Pharmacol. Toxicol. *41*, 471–505.

Horton, A.C., Racz, B., Monson, E.E., Lin, A.L., Weinberg, R.J., and Ehlers, M.D. (2005). Polarized secretory trafficking directs cargo for asymmetric dendrite growth and morphogenesis. Neuron *48*, 757–771.

Huang, E.J., and Reichardt, L.F. (2003). Trk receptors: roles in neuronal signal transduction. Annu. Rev. Biochem. *72*, 609–642.

Huang, K., and El-Husseini, A. (2005). Modulation of neuronal protein trafficking and function by palmitoylation. Curr. Opin. Neurobiol. *15*, 527–535.

Hudmon, A., and Schulman, H. (2002). Neuronal Ca^{2+}/Calmodulin-dependent protein kinase II: the role of structure and autoregulation in cellular function. Annu. Rev. Biochem. *71*, 473–510.

Jan, Y.-N., and Jan, L.Y. (2003). The control of dendrite development. Neuron *40*, 229–242.

Kawauchi, T., Chihama, K., Nabeshima, Y., and Hoshino, M. (2003). The in vivo roles of STEF/Tiam1, Rac1 and JNK in cortical neuronal migration. EMBO J. *22*, 4190–4201.

Keller, C.A., Yuan, X., Panzanelli, P., Martin, M.L., Alldred, M., Sassoe-Pognetto, M., and Luscher, B. (2004). The gamma2 subunit of $GABA_A$ receptors is a substrate for palmitoylation by GODZ. J. Neurosci. *24*, 5881–5891.

Kennedy, M.B. (2000). Signal-processing machines at the postsynaptic density. Science *290*, 750–754.

Konur, S., and Ghosh, A. (2005). Calcium signaling and the control of dendritic development. Neuron *46*, 401–405.

Kozorovitskiy, Y., Gross, C.G., Kopil, C., Battaglia, L., McBreen, M., Stranahan, A.M., and Gould, E. (2005). Experience induces structural and biochemical changes in the adult primate brain. Proc. Natl. Acad. Sci. USA *102*, 17478–17482.

Kuhn, T.B., Williams, C.V., Dou, P., and Kater, S.B. (1998). Laminin directs growth cone navigation via two temporally and functionally distinct calcium signals. J. Neurosci. *18*, 184–194.

Kumanogoh, H., Miyata, S., Sokawa, Y., and Maekawa, S. (2001). Biochemical and morphological analysis on the localization of Rac1 in neurons. Neurosci. Res. *39*, 189–196.

Linder, M.E., and Deschenes, R.J. (2004). Model organisms lead the way to protein palmitoyltransferases. J. Cell Sci. *117*, 521–526.

Lisman, J., Schulman, H., and Cline, H. (2002). The molecular basis of CaMKII function in synaptic and behavioural memory. Nat. Rev. Neurosci. *3*, 175–190.

Luo, L. (2002). Actin cytoskeleton regulation in neuronal morphogenesis and structural plasticity. Annu. Rev. Cell Dev. Biol. *18*, 601–635.

Matsuo, N., Hoshino, M., Yoshizawa, M., and Nabeshima, Y. (2002). Characterization of STEF, a guanine nucleotide exchange factor for Rac1, required for neurite growth. J. Biol. Chem. *277*, 2860–2868.

Meijering, E., Jacob, M., Sarria, J.C., Steiner, P., Hirling, H., and Unser, M. (2004). Design and validation of a tool for neurite tracing and analysis in fluorescence microscopy images. Cytometry A *58*, 167–176.

Mishina, M., and Sakimura, K. (2007). Conditional gene targeting on the pure C57BL/6 genetic background. Neurosci. Res., in press. Published online January 18, 2007. 10.1016/j.neures.2007.01.004.

Miyoshi, H., Blomer, U., Takahashi, M., Gage, F.H., and Verma, I.M. (1998). Development of a self-inactivating lentivirus vector. J. Virol. *72*, 8150–8157.

Nishimura, H., Sakagami, H., Uezu, A., Fukunaga, K., Watanabe, M., and Kondo, H. (2003). Cloning, characterization and expression of two alternatively splicing isoforms of Ca^{2+}/calmodulin-dependent protein kinase I gamma in the rat brain. J. Neurochem. *85*, 1216–1227.

Ohmae, S., Takemoto-Kimura, S., Okamura, M., Adachi-Morishima, A., Nonaka, M., Fuse, T., Kida, S., Tanji, M., Furuyashiki, T., Arakawa, Y., et al. (2006). Molecular identification and characterization of a family of kinases with homology to Ca2+/calmodulin-dependent protein kinases I/IV. J. Biol. Chem. *281*, 20427–20439.

Pelled, D., Riebeling, C., van Echten-Deckert, G., Sandhoff, K., and Futerman, A.H. (2003). Reduced rates of axonal and dendritic growth in embryonic hippocampal neurones cultured from a mouse model of Sandhoff disease. Neuropathol. Appl. Neurobiol. *29*, 341–349.

Redmond, L., Kashani, A.H., and Ghosh, A. (2002). Calcium regulation of dendritic growth via CaM Kinase IV and CREB-mediated transcription. Neuron *34*, 999–1010.

Schmitt, J.M., Wayman, G.A., Nozaki, N., and Soderling, T.R. (2004). Calcium activation of ERK mediated by calmodulin kinase I. J. Biol. Chem. *279*, 24064–24072.

Schmitt, J.M., Guire, E.S., Saneyoshi, T., and Soderling, T.R. (2005). Calmodulin-dependent kinase kinase/calmodulin kinase I activity gates extracellular-regulated kinase-dependent long-term potentiation. J. Neurosci. *25*, 1281–1290.

Schwarz, A., and Futerman, A.H. (1998). Inhibition of sphingolipid synthesis, but not degradation, alters the rate of dendrite growth in cultured hippocampal neurons. Brain Res. Dev. Brain Res. *108*, 125–130.

Silva, A.J., Kogan, J.H., Frankland, P.W., and Kida, S. (1998). CREB and memory. Annu. Rev. Neurosci. *21*, 127–148.

Soderling, T.R., and Stull, J.T. (2001). Structure and regulation of calcium/calmodulin-dependent protein kinases. Chem. Rev. *101*, 2341–2352.

Suzuki, T., Ito, J., Takagi, H., Saitoh, F., Nawa, H., and Shimizu, H. (2001). Biochemical evidence for localization of AMPA-type glutamate receptor subunits in the dendritic raft. Brain Res. Mol. Brain Res. *89*, 20–28.

Suzuki, S., Numakawa, T., Shimazu, K., Koshimizu, H., Hara, T., Hatanaka, H., Mei, L., Lu, B., and Kojima, M. (2004). BDNF-induced recruitment of TrkB receptor into neuronal lipid rafts: roles in synaptic modulation. J. Cell Biol. *167*, 1205–1215.

Takemoto-Kimura, S., Terai, H., Takamoto, M., Ohmae, S., Kikumura, S., Segi, E., Arakawa, Y., Furuyashiki, T., Narumiya, S., and Bito, H. (2003). Molecular cloning and characterization of CLICK-III/CaMKIgamma, a novel membrane-anchored neuronal Ca^{2+}/calmodulin-dependent protein kinase (CaMK). J. Biol. Chem. *278*, 18597–18605.

Tolias, K.F., Bikoff, J.B., Burette, A., Paradis, S., Harrar, D., Tavazoie, S., Weinberg, R.J., and Greenberg, M.E. (2005). The Rac1-GEF Tiam1 couples the NMDA receptor to the activity-dependent development of dendritic arbors and spines. Neuron *45*, 525–538.

Uemura, T., Mori, H., and Mishina, M. (2002). Isolation and characterization of Golgi apparatus-specific GODZ with the DHHC zinc finger domain. Biochem. Biophys. Res. Commun. *296*, 492–496.

Vaillant, A.R., Zanassi, P., Walsh, G.S., Aumont, A., Alonso, A., and Miller, F.D. (2002). Signaling mechanisms underlying reversible, activity-dependent dendrite formation. Neuron *34*, 985–998.

Van Aelst, L., and Cline, H.T. (2004). Rho GTPases and activity-dependent dendrite development. Curr. Opin. Neurobiol. *14*, 297–304.

Wassif, C.A., Zhu, P., Kratz, L., Krakowiak, P.A., Battaile, K.P., Weight, F.F., Grinberg, A., Steiner, R.D., Nwokoro, N.A., Kelley, R.I., et al. (2001). Biochemical, phenotypic and neurophysiological characterization of a genetic mouse model of RSH/Smith-Lemli-Opitz syndrome. Hum. Mol. Genet. *10*, 555–564.

Wayman, G.A., Kaech, S., Grant, W.F., Davare, M., Impey, S., Tokumitsu, H., Nozaki, N., Banker, G., and Soderling, T.R. (2004). Regulation of axonal extension and growth cone motility by calmodulin-dependent protein kinase I. J. Neurosci. *24*, 3786–3794.

Wayman, G.A., Impey, S., Marks, D., Saneyoshi, T., Grant, W.F., Derkach, V., and Soderling, T.R. (2006). Activity-dependent dendritic arborization mediated by CaM-kinase I activation and enhanced CREB-dependent transcription of Wnt-2. Neuron *50*, 897–909.

Whitford, K.L., Dijkhuizen, P., Polleux, F., and Ghosh, A. (2002). Molecular control of cortical dendrite developement. Annu. Rev. Neurosci. *25*, 127–149.

Wu, G.-Y., and Cline, H.T. (1998). Stabilization of dendritic arbor structure in vivo by CaMKII. Science *279*, 222–226.

Yu, X., and Malenka, R.C. (2003). Beta-catenin is critical for dendritic morphogenesis. Nat. Neurosci. *6*, 1169–1177.

Zacharias, D.A., Violin, J.D., Newton, A.C., and Tsien, R.Y. (2002). Partitioning of lipid-modified monomeric GFPs into membrane microdomains of live cells. Science *296*, 913–916.

Zheng, J.Q., Felder, M., Connor, J.A., and Poo, M.M. (1994). Turning of nerve growth cones induced by neurotransmitters. Nature *368*, 140–144.

nature neuroscience

ARTICLES

RIM1 confers sustained activity and neurotransmitter vesicle anchoring to presynaptic Ca^{2+} channels

Shigeki Kiyonaka[1], Minoru Wakamori[1], Takafumi Miki[1], Yoshitsugu Uriu[1], Mio Nonaka[2], Haruhiko Bito[2], Aaron M Beedle[3], Emiko Mori[1], Yuji Hara[1,3], Michel De Waard[4], Motoi Kanagawa[3], Makoto Itakura[5], Masami Takahashi[5], Kevin P Campbell[3] & Yasuo Mori[1]

The molecular organization of presynaptic active zones is important for the neurotransmitter release that is triggered by depolarization-induced Ca^{2+} influx. Here, we demonstrate a previously unknown interaction between two components of the presynaptic active zone, RIM1 and voltage-dependent Ca^{2+} channels (VDCCs), that controls neurotransmitter release in mammalian neurons. RIM1 associated with VDCC β-subunits via its C terminus to markedly suppress voltage-dependent inactivation among different neuronal VDCCs. Consistently, in pheochromocytoma neuroendocrine PC12 cells, acetylcholine release was significantly potentiated by the full-length and C-terminal RIM1 constructs, but membrane docking of vesicles was enhanced only by the full-length RIM1. The β construct beta-AID dominant negative, which disrupts the RIM1-β association, accelerated the inactivation of native VDCC currents, suppressed vesicle docking and acetylcholine release in PC12 cells, and inhibited glutamate release in cultured cerebellar neurons. Thus, RIM1 association with β in the presynaptic active zone supports release via two distinct mechanisms: sustaining Ca^{2+} influx through inhibition of channel inactivation, and anchoring neurotransmitter-containing vesicles in the vicinity of VDCCs.

The presynaptic active zone is the specific site for impulse-evoked exocytosis of neurotransmitters at synapses of the nervous system in a wide variety of species[1,2]. Fine regulation of presynaptic active zone neurotransmitter release is integral to nervous system adaptive functions, including learning, memory and cognition. The molecular organization of presynaptic active zones, where synaptic vesicles are docked in close vicinity to VDCCs at the presynaptic membrane, is essential for controlling the neurotransmitter release triggered by depolarization-induced Ca^{2+} influx. The spacing between VDCCs and vesicles influences the dynamic properties of synaptic transmission[3]. However, the molecular determinants that maintain vesicles and VDCCs within a physiologically appropriate distance have remained elusive.

Originally identified as a putative effector for the synaptic vesicle protein Rab3 (ref. 4), RIM1 is part of the RIM superfamily, whose members share a common C_2B domain at their C termini[5]. RIM1 interacts with other presynaptic active zone protein components, including Munc13, ELKS (also known as CAST), RIM-BP and liprins, to form a protein scaffold in the presynaptic nerve terminal[6–10]. Mouse knockouts showed that, in different types of synapses, RIM1 is essential for different forms of synaptic plasticity[9,11]. In the CA1-region Schaffer-collateral excitatory synapses and GABAergic synapses, RIM1 maintains normal neurotransmitter release and short-term synaptic plasticity. In excitatory CA3-region mossy fiber synapses and cerebellar parallel fiber synapses, RIM1 is necessary for presynaptic long-term synaptic plasticity. In autapses, the RIM1 deletion significantly reduces the readily releasable pool of vesicles, and it alters short-term plasticity and the properties of evoked asynchronous release[12]. However, in spite of this progress in understanding RIM1 functions, the mechanisms by which RIM1 acts remain unknown. Moreover, the physiological functions of other RIM isoforms (RIM2, RIM3 and RIM4)[5] remain unclear.

Multiple types of VDCCs that are distinguished on the basis of biophysical and pharmacological properties coexist in neurons[13]. High voltage–activated types of VDCCs that are essential for neurotransmitter release include N-, P/Q-, R- and L-types[14–16]. VDCCs are heteromultimeric protein complexes composed of the pore-forming α_1, designated as Ca_v, and auxiliary subunits α_2/δ, β and γ[17]. The α_1 subunit is encoded by ten distinct genes, whose correspondence with functional types is largely elucidated[13,17]. VDCC complexes are associated, primarily via interactions with the α_1 subunit[18–25], with presynaptic and postsynaptic proteins including syntaxin, SNAP-25, synaptotagmin, CASK and Mint. The α_1 and β subunits interact to enhance functional channel trafficking to the plasma membrane[26,27]

[1]Department of Synthetic Chemistry and Biological Chemistry, Graduate School of Engineering, Kyoto University, Katsura Campus, Nishikyo-ku, Kyoto 615-8510, Japan. [2]Department of Neurochemistry, University of Tokyo Graduate School of Medicine, Hongo 7-3-1, Bunkyo-ku, Tokyo 113-0033, Japan. [3]Howard Hughes Medical Institute and Departments of Physiology and Biophysics, Internal Medicine, and Neurology, University of Iowa Roy J. and Lucille A. Carver College of Medicine, 285 Newton Road, Iowa City, Iowa 52242-1101, USA. [4]Inserm U607, Laboratoire Canaux Calciques, Fonctions et Pathologies, 17 Rue des Martyrs, Bâtiment C3, 38054 Grenoble Cedex 09, France. [5]Department of Biochemistry, Kitasato University School of Medicine, Kitasato 1-15-1, Sagamihara, Kanagawa 228-8555, Japan. Correspondence should be addressed to Y.M. (mori@sbchem.kyoto-u.ac.jp).

Received 23 February; accepted 2 April; published online 13 May 2007; doi:10.1038/nn1904

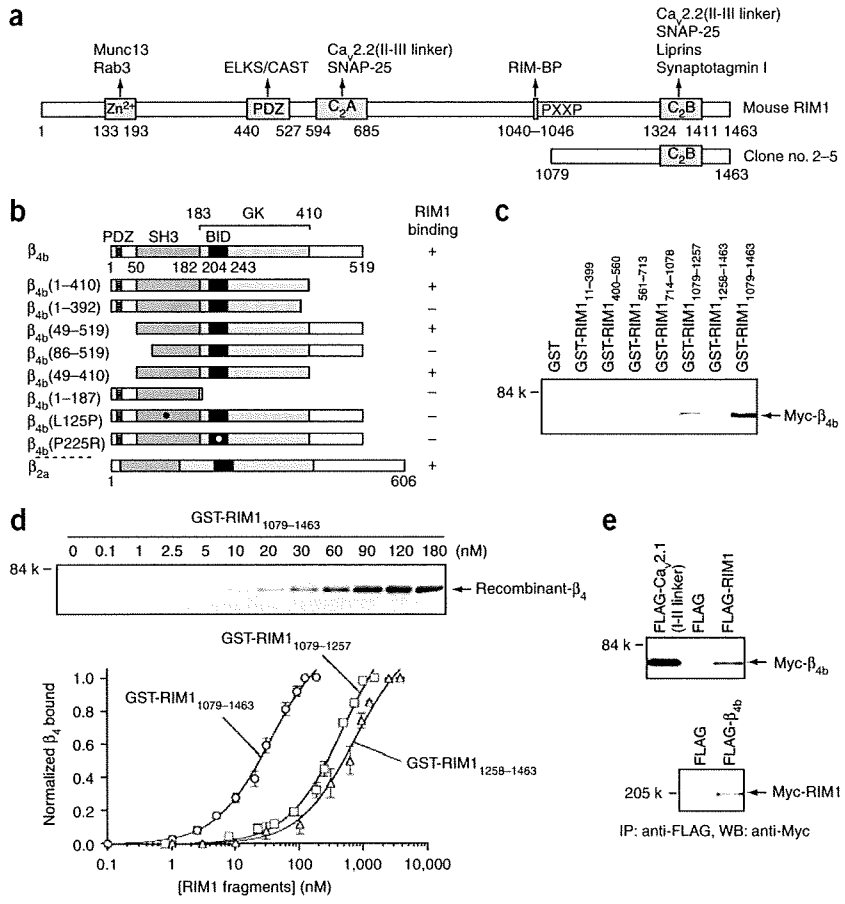

Figure 1 Direct interaction of RIM1 with the VDCC β_{4b} subunit. **(a)** Domain structure of mouse RIM1. Arrows indicate molecules interacting with RIM1 at the Zn^{2+}-finger–like domain (Zn^{2+}), PDZ domain (PDZ), first and second C_2 domains (C_2A and C_2B) and proline-rich region (PXXP)[4,6–10]. The protein region encoded by clone no. 2–5 is also indicated. **(b)** Mapping of RIM1-binding sites on β_{4b} by the yeast two-hybrid assay. β-subunit constructs in bait vectors were tested with RIM1 in the prey vector. The interactions were scored by β-galactosidase activity and His^+ prototrophy. **(c)** Pulldown assay of β_{4b} with GST fusion RIM1 mutants. GST fusion proteins immobilized on glutathione-Sepharose beads were incubated with cell lysates obtained from Myc-β_{4b}–transfected HEK293 cells. Bound proteins were analyzed by western blotting (WB) using antibody for Myc. **(d)** *In vitro* association between the purified GST-RIM1 fusion constructs and recombinant β_4 subunit (residues 47–475). GST-RIM1 proteins at various concentrations, incubated with β_4 (50 pM), were captured by glutathione-Sepharose beads. Captured β_4 proteins were examined by WB. The bottom panel shows the quantitative densitometric analysis of bands shown in the upper panel and in **Supplementary Figure 2**. The saturation curves were subjected to the nonlinear least-squares curve-fitting method to evaluate the apparent dissociation constant (K_d). k, kDa. **(e)** Interaction of recombinant β_{4b} and RIM1 in HEK293 cells. The interaction is evaluated by immunoprecipitation (IP) with antibody for FLAG, followed by WB with antibody for Myc. Top, physical association of Myc-β_{4b} with FLAG-RIM1 in comparison with a positive control FLAG-$Ca_v2.1$(I-II linker). Bottom, physical association of FLAG-β_{4b} with Myc-RIM1.

and to modify multiple kinetic properties[28]; the β subunit also interacts with other proteins[29–31]. Therefore, it is intriguing to investigate whether β subunits are involved in targeting VDCC complexes to specific subcellular machinery at presynaptic active zones for neurotransmitter release through as yet unidentified interactions. Here, we demonstrate a previously unknown molecular interaction between RIM1 and VDCC β subunits, both of which are essential presynaptic active zone proteins. The RIM1-β interaction supports the function of RIM1 in neurotransmitter release via two distinct mechanisms: the anchoring of neurotransmitter-containing vesicles in the vicinity of VDCCs, and the sustenance of Ca^{2+} influx through the inhibition of voltage-dependent inactivation.

RESULTS

VDCC β subunits directly interact with RIM1

To identify β subunit–interacting proteins that regulate presynaptic active zone organization, we performed yeast two-hybrid screening with a mouse brain complementary DNA library using the full-length rat β_{4b} subunit as a bait. The β_4 subunit was chosen because spontaneous β_4 mutant *Cacnb4*^{lh} (lethargic) mice[32] have clear neurological defects suggesting that β_4-containing VDCCs are physiologically significant in the brain. Screening identified a clone (no. 2-5) encoding the C-terminal region (residues 1079–1463) of the mouse RIM1 protein[4] including the C_2B domain (**Fig. 1a**). Subsequent two-hybrid assays using β_{4b} mutants showed that residues 49–410, containing major structural motifs such as the Src homology 3 (SH3) domain, the α_1-interacting domain known as BID and the guanylate kinase (GK) domain, were required for the interaction of β_{4b} with the RIM1 C terminus (**Fig. 1b**). β_{2a} also showed RIM1 interaction. *In vitro* pulldown assays using glutathione-*S*-transferase (GST) fusion constructs identified the RIM1 C terminus (residues 1079–1463) as a major β_4-interaction domain likely formed in concert by two adjacent subdomains (1079–1257 and 1258–1463; **Fig. 1c** and **Supplementary Fig. 1** online). An *in vitro* binding assay using purified β_4 and RIM1 recombinants revealed a dissociation constant (K_d) of 35.1 nM for $RIM1_{1079–1463}$, which was substantially lower than those of $RIM1_{1079–1257}$ (481 nM) and $RIM1_{1258–1463}$ (717 nM) (**Fig. 1d** and **Supplementary Fig. 2** online). These results, as well as the successful coimmunoprecipitation of full-length RIM1 with β_{4b} (**Fig. 1e**), suggest that a direct protein-protein interaction occurs between RIM1 and β_4.

RIM1 physically associates with native VDCCs in the brain

We characterized the association between native VDCCs and RIM1 biochemically using VDCC complexes enriched from mouse brains through microsome preparation, KCl wash, solubilization, heparin purification and sucrose density gradient fractionation[25]. Western blot analysis of sucrose gradient fractions showed cosedimentation of RIM1 with $Ca_v2.1$ and β_4 (**Fig. 2a**). Statistical analysis of cosedimentation data revealed a complete overlap of $Ca_v2.1$ and β_4, confirming that they associate in the VDCC complex (**Fig. 2b**). RIM1 sedimented in overlapping minor and major peaks: the latter completely overlapped with VDCC subunits, whereas the former did not cosediment with VDCC and is likely to represent a subset of RIM1 in a smaller,

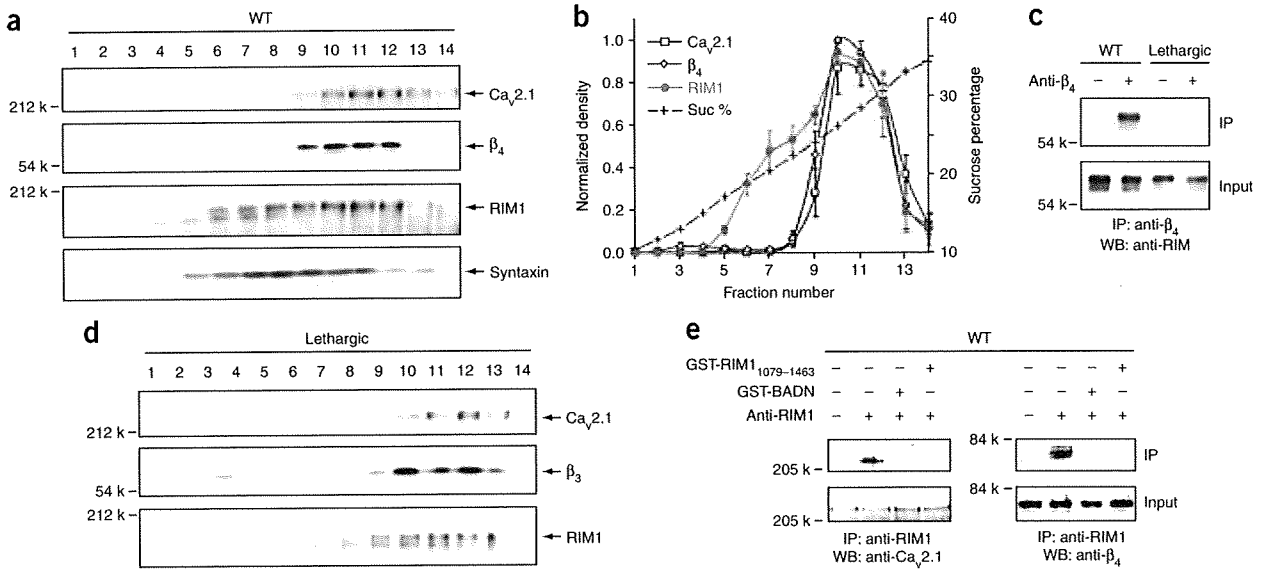

Figure 2 Association of RIM1 with native neuronal VDCC complexes. **(a)** Sucrose gradient fractionation of neuronal VDCC complexes from wild-type (WT) mouse brains and subsequent western blot (WB) showed cosedimentation of RIM1 with $Ca_V2.1$ and β_4. Syntaxin showed similar cosedimentation with RIM1. **(b)** Densitometry of $Ca_V2.1$, β_4 and RIM1 from western blots of sucrose gradient fractions. The normalized density of each protein is plotted as a function of the sucrose density fraction number. **(c)** Coimmunoprecipitation of RIM1 with the β_4 subunit. Immunoprecipitation (IP) using an antibody for β_4 and subsequent WB for RIM1 was carried out on heparin-purified samples. A preparation from lethargic mice was used as a negative control. **(d)** Sucrose gradient fractionation of neuronal VDCC complexes from lethargic mouse brains. **(e)** Coimmunoprecipitation of VDCC subunits with RIM1. The immunocomplexes were disrupted by GST-BADN or GST-RIM1$_{1079-1463}$. IP using anti-RIM1 antibody and subsequent western blotting for $Ca_V2.1$ or β_4 was carried out.

non-VDCC complex. Syntaxin, a VDCC-interacting protein[18–21], showed similar cosedimentation with RIM1. Immunoprecipitation analysis of heparin-purified samples confirmed that the cosedimentation of RIM1 is due to its specific interaction with VDCC subunits (**Fig. 2c**). Antibody specific for β_4 precipitated RIM1 from wild-type mice, but not from lethargic mice (which carry a mutated form of the gene *Cacnb4*), expressing truncated β_4 protein lacking the α_1-interacting region[32,33]. It is unlikely that the β_4 isoform exclusively mediates the RIM1-VDCC association in the brain, as wild-type and lethargic mice were indistinguishable in the sucrose gradient profile (**Fig. 2d**). We designed a dominant-negative suppressor β_{4b} fusion construct (beta-AID dominant negative, BADN) to dissociate the activity of β-binding proteins such as RIM1 from the functional VDCC complex (**Supplementary Fig. 3** online). As residues 49–410 of the entire 519-amino-acid β_{4b} sequence are required for RIM1 binding (**Fig. 1b**), BADN was designed from the 'full-length' β_{4b} to efficiently quench RIM1. BADN also carries the β-interacting AID region from $Ca_V2.1$ buried at the α_1-binding site[33]. Because the intermolecular association of BADN with VDCC α_1 is inhibited by the intramolecular occlusion of the α_1-binding site in BADN, overexpression of BADN should deprive native β subunits of RIM1 without affecting their association with α_1. *In vitro* binding and coimmunoprecipitation experiments showed that BADN could bind to RIM1, but not to the AID-containing I-II linker region of $Ca_V2.1$ (**Supplementary Fig. 3**). Notably, the native RIM1-β association in partially purified brain VDCCs was disrupted by an 8-h co-incubation with 100 nM GST fusion proteins for BADN or RIM1$_{1079-1463}$ (**Fig. 2e**). *In vitro* binding of β_4 to RIM1$_{1079-1463}$ rapidly decayed with the addition of excess BADN (200 nM), indicating that this disruption is attributable to displacement of binding partners in the native association (**Supplementary Fig. 3**). These results provide evidence for a physiological association between native RIM1 and P/Q-type VDCCs via the β subunit in brain.

RIM1 targets to VDCC via β subunits at the plasma membrane

In recombinant HEK293 cells, β_{4b} and RIM1 were concentrated at the plasma membrane when they were coexpressed with the P/Q-type $Ca_V2.1$ α_1 subunit, whereas they were diffusively colocalized throughout the intracellular area in the absence of $Ca_V2.1$ (**Fig. 3a** and **Supplementary Fig. 4** online). The ratio of the fluorescence intensity at the plasma membrane, PM, to that in the cytoplasm, CYT—F_{PM}/F_{CYT}—was 0.52 ± 0.07 and 0.48 ± 0.07 with $Ca_V2.1$ and 0.10 ± 0.02 and 0.08 ± 0.02 without $Ca_V2.1$ for β_{4b} and RIM1, respectively. RIM1 localization to the plasma membrane via a membrane-targeted β-binding domain[27] composed of CD8 and the $Ca_V2.1$ I-II linker was elicited only after β_{4b} expression (**Fig. 3b** and **Supplementary Fig. 4**). The F_{PM}/F_{CYT} ratio was 0.29 ± 0.03 and 0.27 ± 0.02 with β_{4b}, and 0.08 ± 0.01 and 0.08 ± 0.02 without β_{4b} for the $Ca_V2.1$ I-II linker and RIM1, respectively. Notably, both the $Ca_V2.1$-mediated plasma membrane colocalization of RIM1 and β_{4b}, and the β_{4b}-mediated colocalization of RIM1 and the $Ca_V2.1$ I-II linker, were disrupted by BADN. In the presence of BADN, F_{PM}/F_{CYT} was 0.56 ± 0.11 and 0.19 ± 0.04 for β_{4b} and RIM1, respectively; and F_{PM}/F_{CYT} was 0.33 ± 0.04 and 0.13 ± 0.04 for the $Ca_V2.1$ I-II linker and RIM1, respectively. Thus, the RIM1-β_{4b} interaction is likely to be essential for the assembly of RIM1 with VDCC at the plasma membrane.

In cultured hippocampal neurons, RIM1 and β_{4b} both accumulated near presynaptic termini, in parallel with $Ca_V2.1$ clustering. These events had a substantially later onset than synaptogenesis, as shown by the synapsin I clustering observed at 8 days *in vitro* (DIV, **Fig. 3c,d**). Quantitative imaging showed that overexpression of either BADN or the RIM1 C terminus, RIM1$_{1079-1463}$, impaired the $Ca_V2.1$ clustering in presynaptic varicosities (**Fig. 3e,f**). The coincident targeting of RIM1 and β_{4b}, as well as the blockade of $Ca_V2.1$ accumulation by quenching of RIM1 and βs, suggests that the RIM1-β interaction regulates the localization of VDCCs at the presynaptic membrane. Because RIM1

interacts with multiple proteins (**Fig. 1a**), the RIM1 effect observed using BADN and $RIM1_{1079–1463}$ could also be attributed to the quenching of other RIM interactions at different subcellular locations. However, a recent immunostaining study showed that the staining intensities for $Ca_V2.2$ and RIM covary at a giant calyx-type synapse[34], consistent with the idea that they are both components of transmitter release sites.

RIM1-β interaction modulates inactivation of VDCCs

To elucidate the functional significance of direct RIM1-β_4 coupling, we characterized whole-cell Ba^{2+} currents through recombinant VDCCs expressed as $\alpha_1\alpha_2/\delta\beta$ complexes containing various neuronal α_1 subunits: N-type $Ca_V2.2$, P/Q-type $Ca_V2.1$, R-type $Ca_V2.3$ and L-type $Ca_V1.2$ channels in BHK cells. The most prominent RIM1 effect on VDCC currents was observed on inactivation parameters. Inactivation was markedly decelerated in N-, P/Q-, R- and L-type currents (**Fig. 4a,b**). The same set of VDCC types also showed a significant depolarizing shift in the voltage dependence of inactivation (**Fig. 4c,d**; see **Supplementary Table 1** for statistical significance). In P/Q-type currents (with β_{4b}), RIM1 shifted the half-inactivation potential ($V_{0.5}$) by +24.6 mV, eliciting an inactivation curve with a component that was susceptible to inactivation induced at high voltages ($V_{0.5}$ (vector) = −45.9 mV, $V_{0.5}$ (RIM1) = −21.3 mV) and a component that was non-inactivating. In N- and R-type currents, RIM1 provoked a switch in the major phase of biphasic inactivation curves from low voltage induced ($V_{0.5}$ and ratio: −64.5 mV and 0.91 for N, and −78.2 mV and 0.91 for R) to high voltage induced ($V_{0.5}$ and ratio: −20.8 mV and 0.61 for N, and −27.9 mV and 0.53 for R). The L-type inactivation curve remained monophasic; however, the non-inactivating component was significantly augmented by RIM1 (from 0.07 to 0.25; $P < 0.05$). In P/Q-type, similar RIM1 effects on inactivation were observed with all other β subunits tested (**Fig. 4a,c** and **Supplementary Table 2** online). Furthermore, the C-terminal truncated mutants $RIM1_{1079–1463}$ and $RIM1_{1258–1463}$, but not $RIM1_{1079–1257}$, successfully slowed P/Q-type

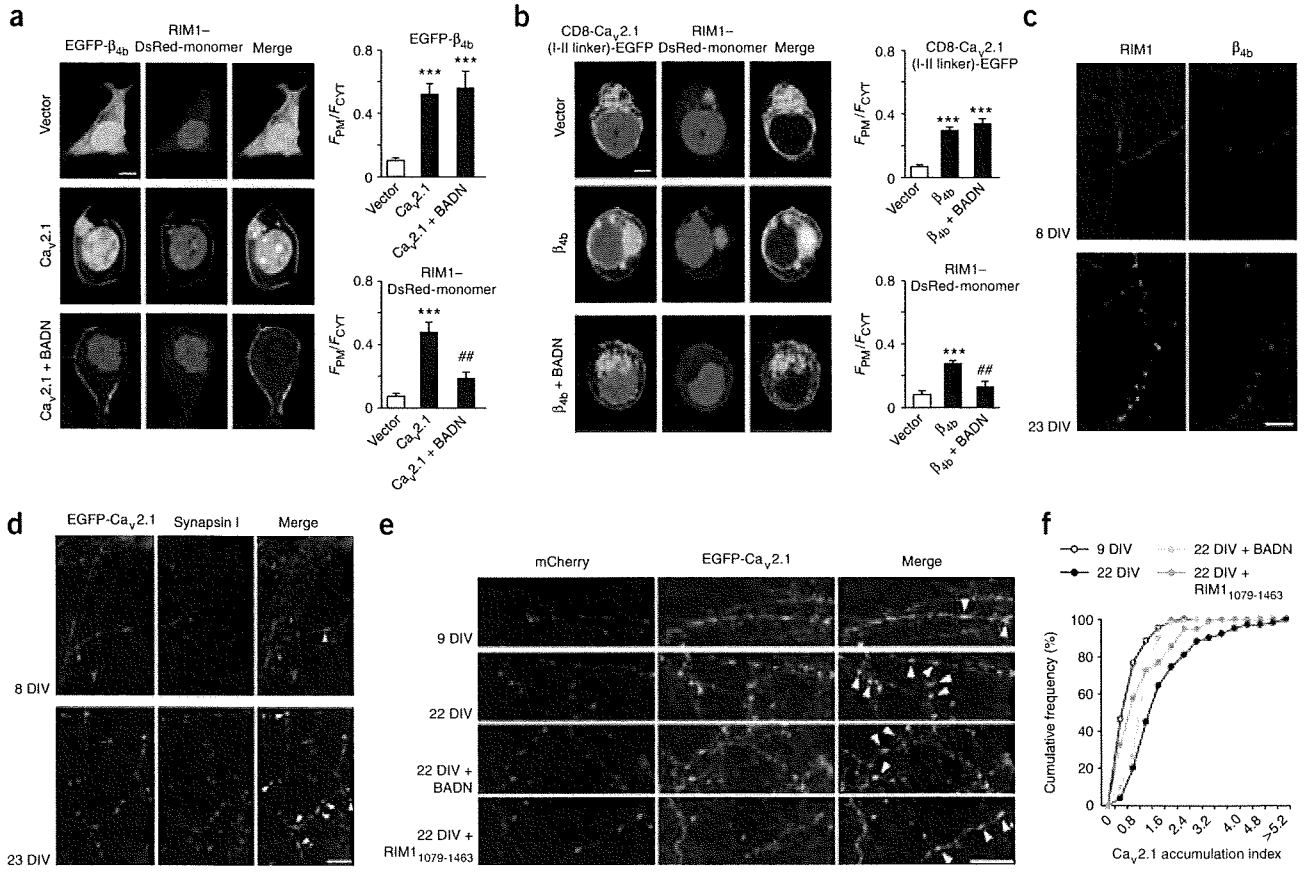

Figure 3 RIM1 clusters with the VDCC subunits near presynaptic termini in cultured hippocampal neurons. (**a**) $Ca_V2.1$ elicited plasma membrane (PM) colocalization of β_{4b} with RIM1. BADN disrupted colocalization. Left, confocal imaging of HEK293 cells expressing EGFP-β_{4b} and RIM1–DsRed-monomer with vector, $Ca_V2.1$ or $Ca_V2.1$ plus BADN. Scale bar, 5 μm. Nuclei were stained with Hoechst 33342. Right, subcellular location of EGFP-β_{4b} or RIM1–DsRed-monomer in 1-μm widths of the plasma membrane region and in the cytosolic area (CYT) ($n = 5$). $^{***}P < 0.001$ versus vector. $^{\#\#}P < 0.01$ versus $Ca_V2.1$. (**b**) β_{4b} elicited plasma membrane colocalization of $Ca_V2.1$(I-II linker) and RIM1. BADN disrupted colocalization. Left, confocal imaging of HEK293 cells expressing CD8-$Ca_V2.1$(I-II linker)-EGFP and RIM1–DsRed-monomer with vector, β_{4b} or β_{4b} and BADN. Right, subcellular location of CD8-$Ca_V2.1$(I-II linker)-EGFP or RIM1–DsRed-monomer ($n = 5$). $^{***}P < 0.001$ versus vector. $^{\#\#}P < 0.01$ versus β_{4b}. (**c**) Immunolocalization of tagged RIM1 and β_{4b} in cultured hippocampal neurons. Clustering of RIM1 and β_{4b} was undetected at 8 DIV, but was present at a substantially later stage at 23 DIV. Scale bar, 10 μm. (**d**) Late clustering of EGFP-$Ca_V2.1$ (arrowheads) in hippocampal neurons. Synapsin I–positive puncta were already abundant at 8 DIV, while $Ca_V2.1$ distribution was still diffuse. Like RIM1 and β_{4b}, $Ca_V2.1$ clustered much later on. (**e,f**) Accumulation of EGFP-$Ca_V2.1$ (arrowheads) in presynaptic varicosities was achieved between 9 and 22 DIV. This maturation process was impaired by $RIM1_{1079–1463}$ or BADN, suggesting that the local VDCC concentration at presynaptic active zones is influenced by RIM1–β-subunit interaction during a postsynaptogenic maturation period.

(with β_{1a}) current inactivation (**Fig. 4a,c** and **Supplementary Table 3** online).

After RIM1 coexpression, single-channel P/Q-type currents clearly showed a prolongation of the mean time between first channel opening and last closing within a trace during 750-ms depolarizations to +20 mV without substantial changes in amplitude (0.59 pA, **Fig. 4e**). This observation corresponds well with the whole-cell data and suggests that RIM1 predominantly stabilizes the non-inactivating

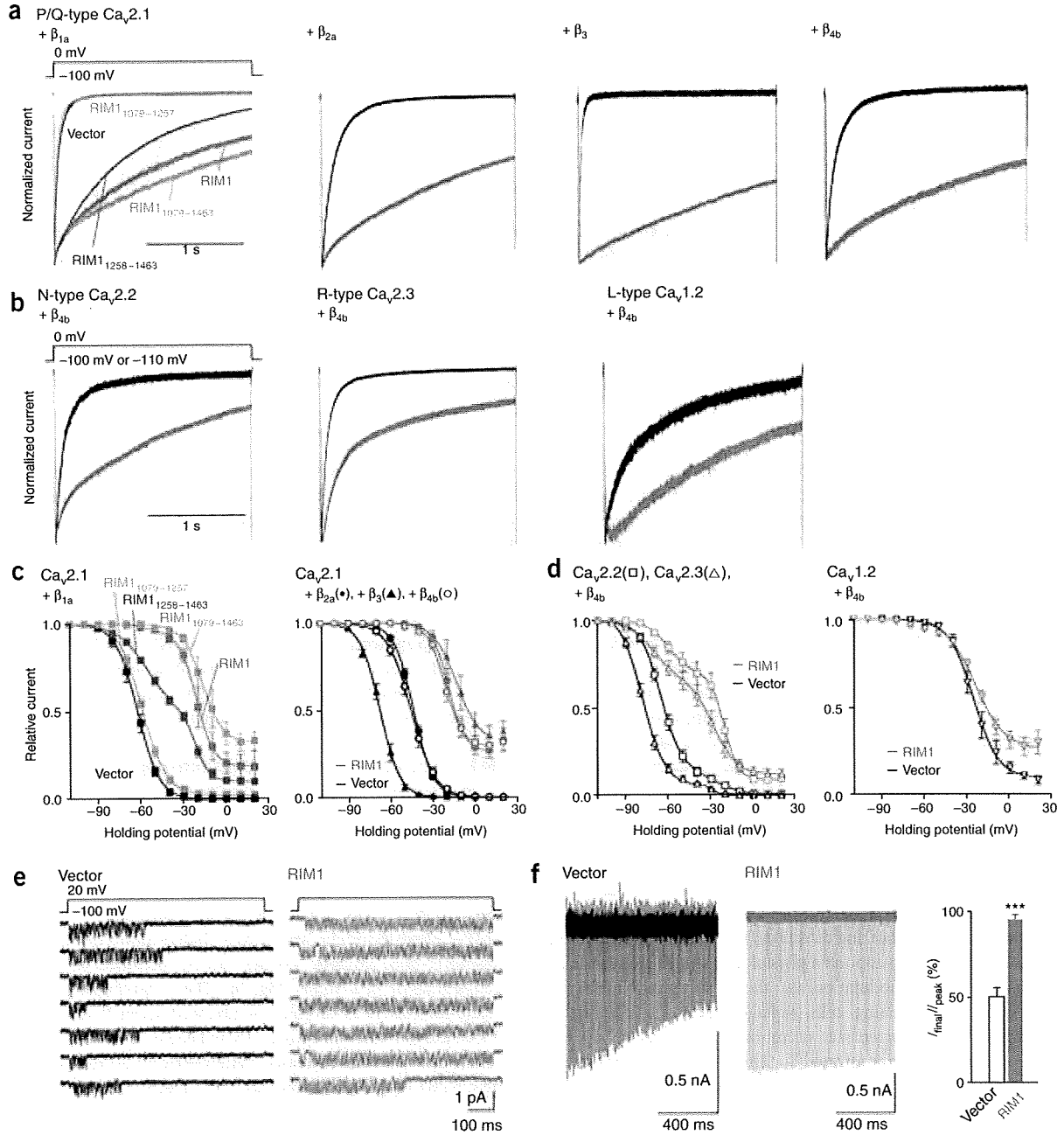

Figure 4 Effects of RIM1 on the inactivation properties of recombinant neuronal VDCCs. (**a**) Inactivation of P/Q-type $Ca_v2.1$ currents in BHK cells. The peak amplitudes before and after coexpression of RIM1 constructs were normalized for Ba^{2+} currents elicited by 2-s pulses to 0 mV from a holding potential (V_h) of −100 mV. (**b**) Inactivation of N-type $Ca_v2.2$, R-type $Ca_v2.3$ or L-type $Ca_v1.2$ currents (with β_{4b}). The V_h was −100 mV ($Ca_v2.2$, $Ca_v1.2$) or −110 mV ($Ca_v2.3$). (**c**) Left, inactivation curves for $Ca_v2.1$ (with β_{1a}). Right, inactivation curves for $Ca_v2.1$ in BHK cells expressing α_2/δ and different β subunits. See **Supplementary Tables 2** and **3** for statistical significance of the differences. (**d**) Inactivation curves for $Ca_v2.2$, $Ca_v2.3$ (left), or $Ca_v1.2$ (right) (with β_{4b}). See **Supplementary Table 1** for statistical significance of the differences. (**e**) RIM1 prolonged the time between first channel opening and last closing within a single-channel trace of $Ca_v2.1$ (with β_{4b}). Seven consecutive unitary traces are shown. The mean values for the time of each trace were 184.2 ± 33.3 ms (n = 117 traces) for vector and 502.8 ± 33.3 ms (n = 101) for RIM1. The time for traces without opening was counted as 0 ms. (**f**) Left, $Ca_v2.1$ currents (with β_{1a}) induced by 100-Hz action potential trains for 1 s. Right, percentage of currents in response to the last stimulus compared with the peak current (n = 6 for vector and n = 4 for RIM1). ***$P < 0.001$.

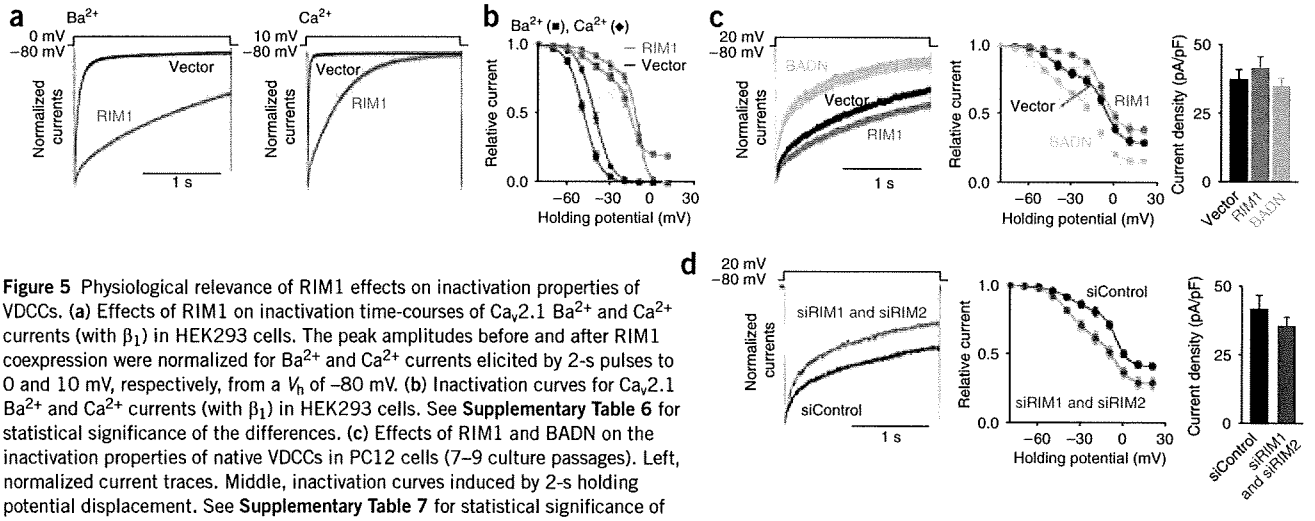

Figure 5 Physiological relevance of RIM1 effects on inactivation properties of VDCCs. (**a**) Effects of RIM1 on inactivation time-courses of $Ca_v2.1$ Ba^{2+} and Ca^{2+} currents (with β_1) in HEK293 cells. The peak amplitudes before and after RIM1 coexpression were normalized for Ba^{2+} and Ca^{2+} currents elicited by 2-s pulses to 0 and 10 mV, respectively, from a V_h of −80 mV. (**b**) Inactivation curves for $Ca_v2.1$ Ba^{2+} and Ca^{2+} currents (with β_1) in HEK293 cells. See **Supplementary Table 6** for statistical significance of the differences. (**c**) Effects of RIM1 and BADN on the inactivation properties of native VDCCs in PC12 cells (7–9 culture passages). Left, normalized current traces. Middle, inactivation curves induced by 2-s holding potential displacement. See **Supplementary Table 7** for statistical significance of the differences. Right, comparison of current densities at 10 mV (n = 18, 15 and 9 cells for vector, RIM1 and BADN, respectively). (**d**) Acceleration of inactivation by application of siRNAs specific for RIM1 and RIM2 (siRIM1 and siRIM2) in VDCC currents recorded from PC12 cells (2–3 culture passages). Left, normalized current traces. Middle, inactivation curves. See **Supplementary Table 7** for statistical significance of the differences. Right, comparison of current densities at 10 mV (n = 6 and 8 cells, for siControl, and siRIM1 and siRIM2, respectively).

mode[35]. Currents evoked by trains of action potential waveforms, a more physiological voltage-clamp protocol used to determine closed-state inactivation[36], further support the existence of a profound suppression of voltage-dependent inactivation by RIM1 (**Fig. 4f**).

The observed effect of RIM1 on VDCC inactivation is attributable to its association with the β subunit, as replacement of β_4 with the C-terminal truncation construct β_4-GK[37], which directly interacts with α_1 but lacks the ability to bind RIM1, did not substantially affect inactivation of N-type currents (**Supplementary Fig. 5** and **Supplementary Table 4** online). In addition, BADN significantly diminished the RIM1 effect on P/Q channel inactivation (**Supplementary Fig. 5** and **Supplementary Table 5** online for statistical significance). When 5 mM Ca^{2+} was used as a physiological charge carrier capable of inducing both Ca^{2+}-dependent and voltage-dependent inactivation[38], RIM1 still exerted prominent suppressive effects on inactivation in P/Q-type currents expressed in HEK293 cells (**Fig. 5a,b** and **Supplementary Table 6** online). Notably, in rat PC12 neuroendocrine cells, BADN or application of siRNAs that specifically suppress RIM1 and RIM2 expression accelerated inactivation and shifted the inactivation curve toward the hyperpolarizing direction (**Fig. 5c,d and Supplementary Table 7** online). This supports a physiologically significant role for RIM-mediated VDCC modulation via the β subunit. Notably, as observed in RIM1-expressing cells, voltage-dependent inactivation of presynaptic VDCC currents at membrane potentials ≥−40 mV has been previously demonstrated[39]. Thus, RIM1 exerts strong suppressive effects on the kinetics and voltage dependence of inactivation of VDCC currents.

RIM1's effects on other functional current parameters such as voltage dependence of activation, activation kinetics and current densities at different voltages in current-voltage relationships differentiate VDCCs into two different groups (**Fig. 6** and **Supplementary Table 1**). In β_{4b}-expressing BHK cells, the current densities of N- and P/Q-type currents were significantly augmented by RIM1, whereas those of R- and L-type currents were unaffected by RIM1 (**Fig. 6c,d**; and see **Supplementary Table 1** for statistical significance). In P/Q-type, $RIM1_{1079–1463}$, which binds β, was sufficient to enhance current density (**Fig. 6c**). By contrast, activation speeds were significantly reduced and activation curves were shifted toward positive potentials by RIM1 in R- and L-types, but not in N- and P/Q-types (**Fig. 6a,b**; and see **Supplementary Table 1** for statistical significance). Replacement of β_{4b} with other β isoforms abolished the augmentation of P/Q-type current densities by RIM1 (**Supplementary Fig. 6** online), but slowed the activation speed of P/Q-type by RIM1 (**Fig. 6b**). The RIM1 positive shift in activation curve was also elicited by β_{2a} in P/Q-type (**Supplementary Fig. 6**). Thus, N- and P/Q-type currents responded differently to RIM1 in terms of activation parameters and current densities than did R- and L-type currents, perhaps reflecting different subcellular localizations or functions of these channel subsets.

RIM1-β binding anchors neurotransmitter vesicles to VDCCs

We directly observed vesicles docked to the plasma membrane using evanescent wave microscopy, which illuminates only the subcellular area from the surface to a depth of less than 100 nm by total internal reflection fluorescence (TIRF). Dense-core vesicles were identified by a fusion protein of neuropeptide Y (NPY) and the fluorescent protein Venus in PC12 cells. The overlapping distribution of NPY-Venus, VAMP–DsRed-monomer and RIM1–DsRed-monomer indicated that transmitter-filled synaptic vesicles can be identified using the fluorescent signals of NPY-Venus (**Fig. 7a**). The codistribution is likely to be specific for RIM1, as caveolin-1–enhanced green fluorescent protein (EGFP) did not colocalize with VAMP–DsRed-monomer. The number of docked vesicles was increased significantly by expression of the full-length RIM1 ($P < 0.001$), whereas it was unaffected by $RIM1_{400–1078}$ or by $RIM1_{11–399}$, which forms a ternary complex with Rab3 and Munc13 via a Zn^{2+} finger critical for neurotransmitter release[40] (**Fig. 7b,c**). BADN, as well as $RIM1_{1079–1463}$, significantly attenuated the number of docked vesicles ($P < 0.001$ for BADN, $P < 0.05$ for $RIM1_{1079–1463}$). These inhibitory effects of BADN and $RIM1_{1079–1463}$ on vesicle docking most likely occur by quenching endogenous full-length RIMs and by saturating RIM1 interaction sites on VDCC β subunits, respectively. The BADN effect is not due to a reduction in the densities of VDCCs in PC12 cells, as BADN did not substantially affect current densities (**Fig. 5c**). Thus, the 'full-length' structure is probably essential for RIM1 to anchor neurotransmitter vesicles to VDCCs.